EARLY WILDFIRE DETECTION WITH LINE SENSORS

A Thesis

presented to

the Faculty of California Polytechnic State University,

San Luis Obispo

In Partial Fulfillment

of the Requirements for the Degree

Master of Science in Electrical Engineering

by

Virginia Yan

March 2021

COMMITTEE MEMBERSHIP

TITLE: Early Wildfire Detection with Line Sensors

AUTHOR: Virginia Yan

DATE SUBMITTED: March 2021

COMMITTEE CHAIR: Majid Poshtan, Ph.D.
Professor of Electrical Engineering

COMMITTEE MEMBER: Joseph Callenes-Sloan, Ph.D.
Professor of Computer Engineering

COMMITTEE MEMBER: Taufik, Ph.D.
Professor of Electrical Engineering

ABSTRACT

Early Wildfire Detection with Line Sensors

Virginia Yan

Over the last few years, wildfires have become more devastating to communities as the fires are inevitably destructive to many homes, businesses, and ecosystems. Frequent wildfires also pose a significant threat to power grids and nearby residents as they can damage transmission lines and other electrical equipment, which in turn can cause major power shutdowns. Especially in western U.S., severe drought conditions and weather variability cause residents to become more vulnerable to wildfire disasters as their safety is threatened. We are incompetent to control the wildfires effectively despite existing advanced technologies. Hence, an algorithm based on energy conservation and heat transfer mechanisms is created to examine the feasibility of line sag sensors to detect wildfires in an early stage. To test the algorithm, it is integrated with a 150-bus synthetic power network using MATLAB. The resulted conductor temperature from randomly selected parameters like fire locations, weather conditions, and fire rate of spread causes the change in line sag over 10 minutes. The line sag behavior is then analyzed under different scenarios. By monitoring real-time power line sag measurements, the analysis shows that early onset wildfires can be detected in less than 3 minutes and up to about 1 km from the power line to the fire. It is also suggested the utilization of silica fabrics on the sensors can provide thermal and fire protection while having no impact to the power line magnetic fields.

Keywords: wildfire, forest fire, detection, line sensors, sag, heat-transfer, FEMM, BehavePlus, MATLAB

ACKNOWLEDGMENTS

I would like to acknowledge and express my sincere gratitude to professors Dr. Majid Poshtan for his invaluable guidance as my advisor. I also thank Dr. Joseph Callenes-Sloan and Dr. Taufik for being in the committee and supporting me throughout the graduate years.

I thank my mother and friends who have always been so supportive for my study. This would not have been possible without their encouragement and understanding.

TABLE OF CONTENTS

LIST OF TABLES

LIST OF FIGURES

Chapter 1

INTRODUCTION

People around the nation have had to deal with wildfire-related effects over the years. Loss of lives, destruction of people's homes, physical health, and mental health are just some of the damages caused by large, and long-lasting wildfires. Utilities have to pay for the damages done to their transmission lines, distribution lines, power transformers, and many other equipment and electrical devices. The 2018 Camp Fire costed at least 85 fatalities, 17 injuries, about 153,000 acres, 18,000 structures, which totaled up to $16.5 billion [22] [51]. The utility company PG&E was responsible for $30 billion in wildfire liabilities because the deadliest fire in California was sparked by the failure of their transmission line.

As communities experience greater variability in weather and drought, these issues are likely to worsen. Without effective fire detection schemes, wildfire events keep happening in different parts of the country every year. For instance, the Saddleridge Fire caused a sequential equipment damage in 2019, destroying 500 kV AC circuits including transmission lines, a major dc flow line, and other electrical devices [27]. Continuous, or sequential fire events continue to increase stress on utility companies to provide quality electrical services. Figure 1.1 is created by mapping the locations of fires and the major transmission lines onto the California map using Google Earth Pro. As shown in Figure 1.1, thousands of wildfire incidents happened in California in 2020. The larger fires are displayed in red circles and labeled, while the red lines represent the major transmission lines in California. It is apparent that majority of the fires occurred in close proximity to the power lines and other electrical equipment. In addition, devastating wildfire incidents have raised a lot of concerns about lack

of preparedness for climate change. Especially in California, the record-breaking wildfires have erupted as a result of the unprecedented drought. The climate change issue needs to be addressed obviously. Meanwhile, the number of wildfires per year also needs to be reduced by utilizing better early fire detection technologies.

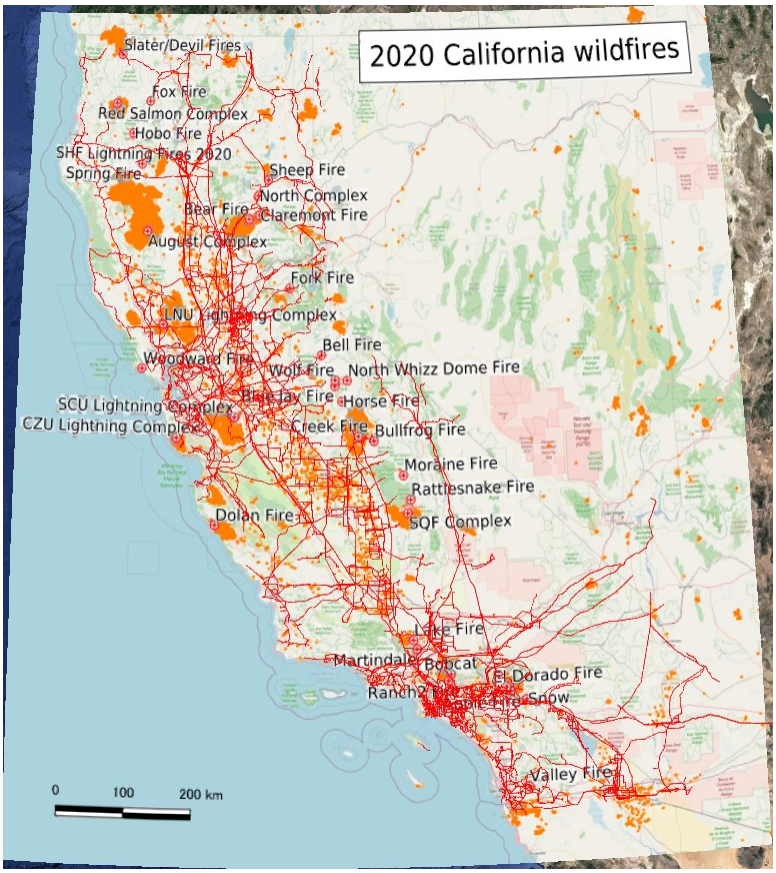

Figure 1.1: California Wildfire Locations and Transmission Lines in 2020.

Detecting wildfires before they start expanding exponentially helps protect residents' safety and prevent more commercial structures and businesses from being destroyed. In addition, it can prevent more spot fires from happening at different locations due to strong wind. Spot fires are created by flying embers and sparks. Without timely response to mitigate the fires, they can pervade through areas with abundant combustible materials. Therefore, detecting wildfires early is important to prevent the fires from transitioning to active crown fires and spreading exponentially;

it is also significant to prevent more spot fires from happening.

As a result, there have been many efforts on the development of wildfire detection technologies, yet a lot of the new technologies or algorithms have disadvantages despite their accuracy or capability in detecting early fires. For instance, satellite imaging systems with machine learning and computer vision algorithms can generally detect fires as small as $100m^2$ [12]. However, such systems are usually costly and may still be insufficient as they cannot help determine how severe a fire is. A better technique would need to be able to analyze the potential damage of the fire before it breaks out and ensure that the fire can be controlled promptly. A more effective and efficient approach is therefore necessary for early wildfire detection.

Facing the challenge of developing a better solution, Sag control is very important in terms of monitoring and detecting any hazards that can spark fires or lead to safety concerns or electrical equipment damage. Line sag can be monitored using technologies like LIDAR or ground laser scanning, or other new measuring devices.

The motivation of this research came from the fact that power grid infrastructures have already spanned many remote areas, and many of these systems contain distributed sensors or dynamic line rating technologies for measuring transmission line temperatures and sag to optimize power flows. As opposed to other methods, the costs are reduced significantly while the accuracy levels are high.

The rest of the paper is organized as follows. Section 2 identifies related research as efforts to improve wildfire detection solutions. In section 3, the approach for leveraging the power grid to detect early onset wildfires is introduced. Then simulation results are presented and discussed in Section 4. Section 5 summarizes the proposed solution to prevent wildfire. Section 6 suggests future improvements.

Chapter 2

BACKGROUND

2.1 Forest Fires

Forest fires happen when ignition starts from either natural environmental reasons like dry, windy days with a high temperature or human actions like fire accidents from parties or barbecue events. Trees, dry wood, and leaves are excellent fuel sources that quickly fuel and help wildfires expand. The initial stage of ignition is surface fire, which only burns dry leaves, twigs, and grass on the ground. When highly combustible fuel sources are abundant and the surface fires have not been controlled, they rapidly feed the adjoining trees and form crown fires.

Crown fires occur where the surface fire intensity is sufficient to ignite tree crowns. The main difference between passive crown fires and active crown fires is that winds are not strong enough to support propagation of the fire from trees to trees in passive crown fires. In contrast, wind conditions are sufficient and encourage the fire to spread to other trees in active crown fires. Figure 2.1 displays the pictures of what the different stages of forest fire ignition look like.

Once the fire transitions to active crown fire from surface fire, it becomes extremely difficult to control and can last for a long period of time if the fuel and weather conditions allow for the expansion.

Millions of acres of land are destroyed by wildfires every year and we have not had good or reliable solutions to the problem besides shutting off electricity prior to the time predicted to have fire-prone weather conditions [25]. There has been much

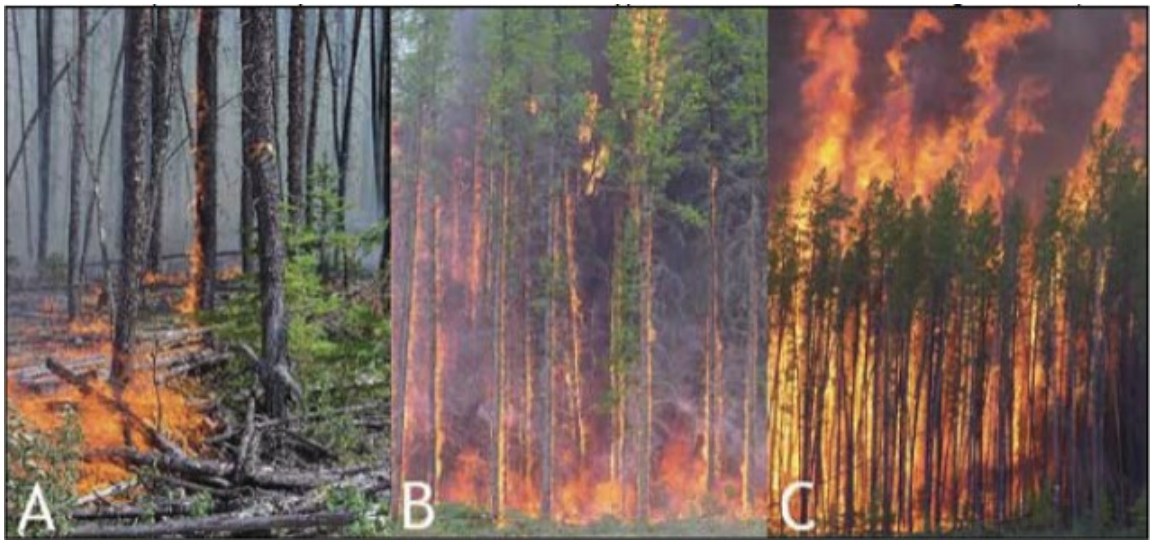

Figure 2.1: Different Stages of Forest Fire Ignition. The forest fire transitions from surface fire to passive and then active crown fire from left to right[41].

research on potential early wildfire detection technologies, and some are currently applied in different countries. However, there needs to be more attention in improving and utilizing some of the techniques throughout the United States. It is important to be able to detect fires in the early stage and notify the operators/fire units as soon as possible.

2.2 Related Work

2.2.1 Spotter Planes

For over twenty years, spotter planes have been commissioned to fly out and keep a lookout for wildfires [42]. Spotter pilots are trained to analyze fire behavior, gather fire information, and communicate with the incident commander on the ground. The incident commander then uses the reported data to make sound decisions to prevent the fire situation from worsening.

Nowadays, spotter aircraft also utilizes different fire detection technologies like camera systems and a detection algorithm to help access the fire situation more effectively and efficiently coordinate with firefighters on the ground.

2.2.2 Satellite Technology

Wildfire detection and monitoring today is conventionally done by manual observation and satellite. Wildfire detection has evolved greatly via the use of satellite technology. MODIS satellites are being used in order to detect, but also primarily to measure the growth and dynamics of wildfires [32]. As of right now, there is a 3-hour satellite detection latency and the average size of a fire that satellites can detect is $1000m^2$. Under near-ideal conditions, fires down to $100m^2$ may also be detected [12]. While our proposed approach is limited in coverage area as compared to satellites, it also has the capability to detect significantly smaller fires and in much shorter periods of time.

2.2.3 Semi-Automated Smoke Detection Systems

Semi-automated smoke detection systems, ForestWatch and Fire Watch are tested and evaluated for their wildfire detection capabilities and coverage ranges [55]. These systems use video cameras that are mounted onto towers. Then motion-change detection algorithms allow the systems to detect smoke and send alert messages to the operator. The operator can then further examine the images captured and make effective decisions to mitigate the fire. With the cameras mounted on communications towers which are about 25 to 30 meters tall, test fires (around 22 m^2 area) are detected at a 10 km range. However, these types of technologies have some disadvantages. For instance, the cameras will fail to detect smoke when they are blocked by tower structures or buildings that are significantly tall. These systems require lookout people at the stations, which means more labor costs in addition to the installation, operation, and maintenance costs of the systems.

2.2.4 Smoke Plume Detection

T. Davenport proposed in his thesis to use texture analysis of principal components from multispectral videos to detect early forest fires [28]. The technique he proposed involves the use of the spectral, temporal, and spatial attributes of a smoke plume for the detection. It uses Principal Component Analysis, a type of eigen decomposition that combines sample data linearly, to capture the temporal and spectral variance of a smoke plume on a sequence of video frames. The texture of the plumes is then characterized by statistical descriptors and it is able to distinguish a smoke plume from other "noise" from its surrounding environment.

2.2.5 Scanning Polarization LIDAR

A scanning polarization LIDAR was developed with the intent to detect early forest fires [29]. J. Xian et all proposed a method to remove obstacle signals through a constructed matrix. The algorithm was able to distinguish the obstacle signals and the fire smoke signals from using the depolarization ratios of obstacles. They were able to reduce the rate of forest fire misidentification and accurately detect a forest fire within a 3-minute duration.

2.2.6 UAV-Based Infrared Cameras

Fixed and Unmanned Aerial Vehicle (UAV)-based infrared cameras and detection algorithms have also been proposed for use in monitoring sites that have particularly high fire risks [28]. Using computer vision these works have been able to detect fire artifacts, such as smoke plumes, with true negative rates over 93% and true positive rates from 60-86% [14]. Using fixed RGB cameras researchers have also shown how smoke plumes from fires as small as $2m^2$ can be detected up to 800 meters away and within 21 seconds of image processing [28]. In this paper, we instead propose an approach that leverages existing power system infrastructure to provide accurate and quick detection without the additional cost of distributed cameras and other equipment. Related work has been done using cameras with neural networks that can detect changes in picture and motion. Such proposed approaches have True Negative Rates of 93.94-99.45% and True Positive Rates of 60.16-86.23%.

2.2.7 Wireless Sensor Network

Wireless sensor network (WSN) is a new technology considered as one of the options in early forest fire detection [13]. An integration of wireless sensors allows it to input physical and chemical parameters that could contribute to a potential fire. Local communications can be done through Zigbee, a communication technology. However, the typical range for Zigbee is between 10 and 20 meters. Although the integrated sensors may be able to maintain low power consumption, they are only designed to carry sensor measurement data over very short distances. This means more installations of sensors, routers, and other devices and hence increases the costs.

2.3 Line Sag Sensors

Modern power grids span remote areas that are highly vulnerable to wildfires and contain sensors, such as temperature and sag sensors, for power monitoring operations. A novel approach was previously proposed to leverage this infrastructure for early fire detection and wildfire dynamic monitoring (e.g., spot fire formation).

Figure 2.2 gives an overview of the primary mechanisms for heat transfer from the early onset wildfire to the power infrastructure, which is created using draw.io. Radiative heat transfers very quickly from the fire to the transmission line and begins to heat the line. Meanwhile, the fire heats the surrounding air that eventually also rises and heats the line. Finally, heat diffuses in the transmission line itself via conduction to raise the temperature of surrounding segments of the line.

Transmission infrastructures increasingly incorporate sensors for monitoring line temperatures and sag in order to better optimize power flows [17, 4]. Dynamic line rating (or real time thermal line rating) is used to measure line ampacity more accu-

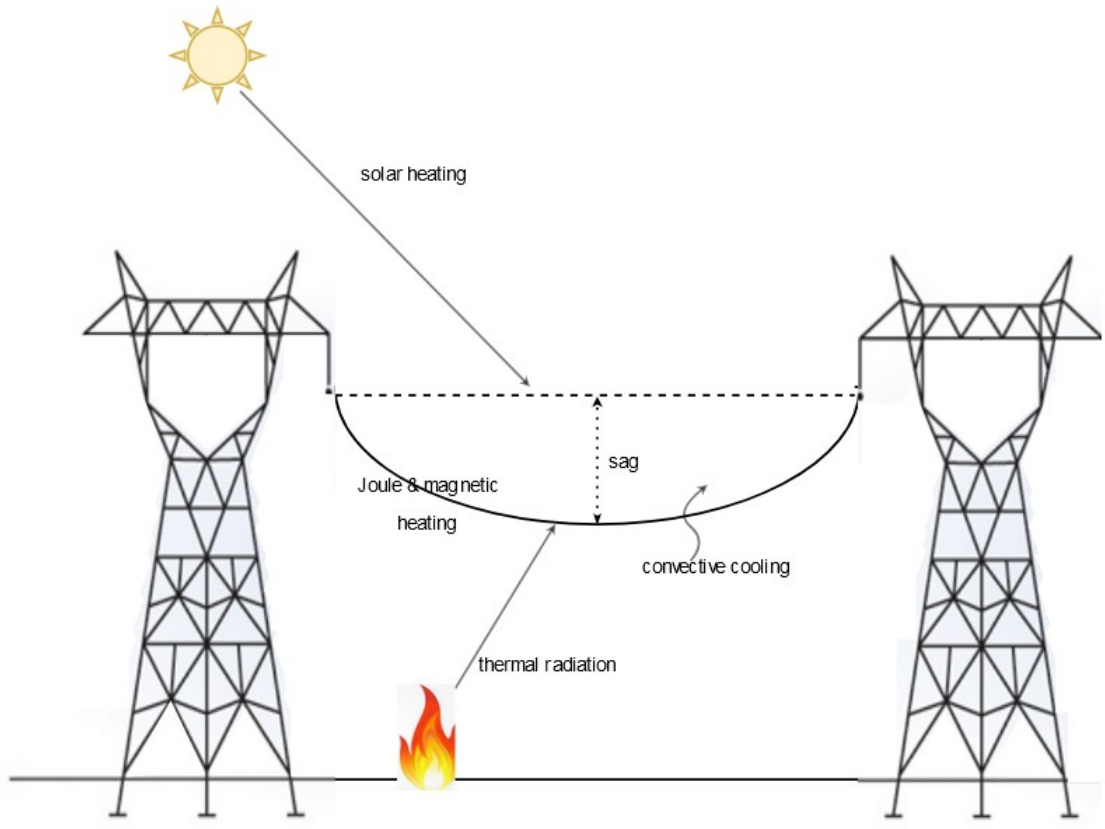

Figure 2.2: Overview of heating dynamics from wildfire to power infrastructure via radiation, conduction, and convection.

rately, and better optimize power flows under varying conditions (e.g., weather and wind). By leveraging line sensors to monitor real-time conditions of power lines, early onset or spot fires can be detected.

The thresholds for alarms depend on system noise and device tolerances. Conventional temperature sensors have a resolution from 0.1 to $2°C$ [63]. Sag sensors using accelerometers to measure the fundamental frequency of the line typically have tolerances within 10 cm [4, 16].

There are around 35,000 miles of transmission and subtransmission lines [1] in California, which equates to approximately 10.5336 billion square meters of land that can be monitored for wildfires using the approach of leveraging existing infrastructure. This amounts to covering approximately 7.88% of all California forest areas (33 million

acres) [6].

The impact of wildfires on power system infrastructures and the effectiveness of the proposed approach are evaluated. A preliminary heat transfer model and simulation show that power line sensors are capable of detecting a potential wildfire happening around a power line. This research uses line sag sensors like Ampacimon's ADR Sense as a reference for the early fire detection analysis.[16].

Chapter 3

METHODOLOGY

This section describes the methods and techniques used to model heat transfer under a fire event and the calculations used to determine the line temperature and sag at the end of the simulation.

Figure 3.1 shows the block diagram of the project, which is created using draw.io. Various inputs are necessary for the heat transfer modeling such as conductor properties and parameters, utility inputs needed to run the load flow study, weather conditions like wind velocities and solar irradiation, and fire parameters. After all these inputs are provided and assumptions are made, the algorithm calculates the conductor temperature over simulation duration, which is then used to determine the line sag over time. The maximum sag is then reported to the incident commander if it violates the sag limit standard or if the line temperature exceeds normal line temperature maximum. Figure 3.2 shows the flow chart of the algorithm and process, which is created using draw.io.

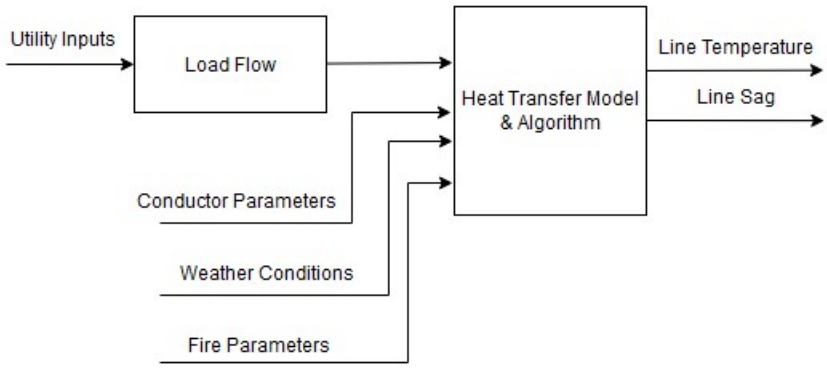

Figure 3.1: Block Diagram.

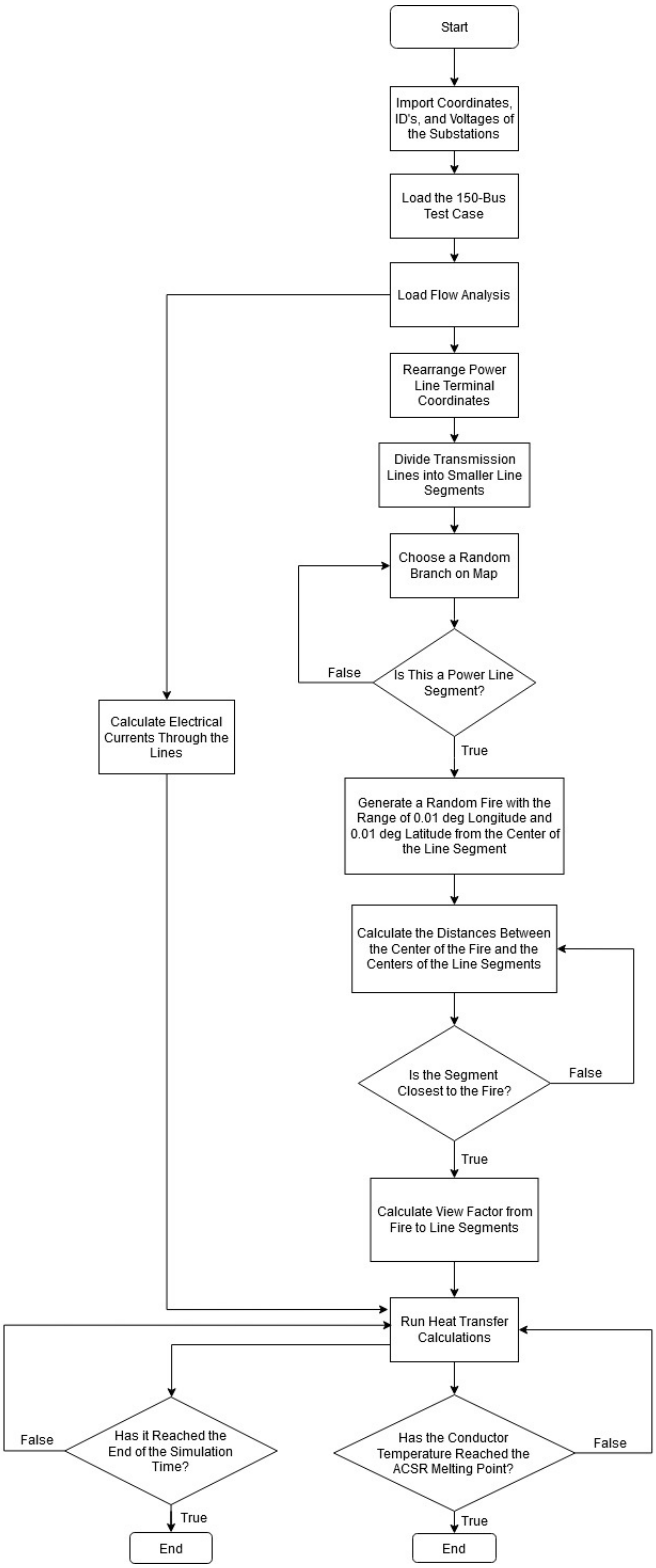

Figure 3.2: Flow Chart of the Algorithm.

3.1 Behaviors of Fire

3.1.1 Fire Expansion Calculation

Wildfires are dynamic and can spread rapidly to other areas that have the perfect wind and fuel conditions like dry, thick vegetation and forests. An estimated rate of fire expansion is considered in this approach, which expands the size of fire overtime [23].

$$sz = 0.5 + 0.36t \tag{3.1}$$

where sz is the area of fire, and t is time in second. This equation suggests that the size of fire is initially 5 m^2 and expands at a rate of 0.36 m/s.

3.2 Power Lines

Bare conductors like AAC, AAAC, ACSR are the most commonly used transmission and distribution lines. AAC stands for All Aluminum Conductor, which consists of one or more bundles of aluminum wires. AAAC is All Aluminum Alloy Conductor and ACSR is Aluminum Conductor Steel Reinforced. AAAC conductors are made from aluminum-magnesium silicon alloy of high electrical conductivity, which provides better weight and strength than other types of conductors. As shown in Figure 3.3, an ACSR conductor is made from a solid or stranded steel core surrounded by strands of aluminum[58]. This type of conductor is very suitable for long spans of transmission lines at different voltage levels due to its high tensile strength, dependability, and low costs. The conductor used in the simulation is the 795 kcmil 26/7 Drake ACSR conductor.

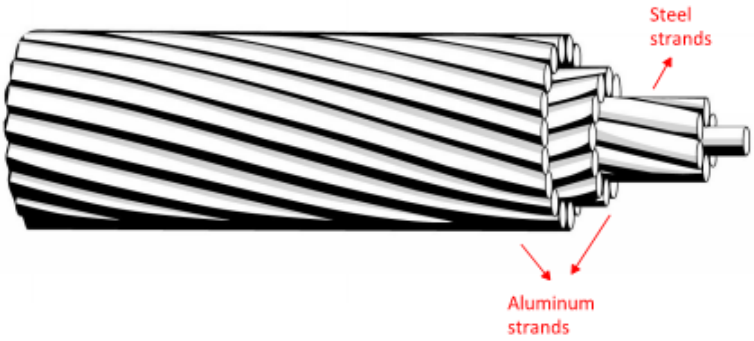

Figure 3.3: Front View of an Aluminum Conductor Steel Reinforced Construction.

3.3 Heat Transfer Theory

There are many factors that contribute to power line temperature change. For instance, weather conditions like ambient temperature, wind velocity, and solar heating parameters usually change in time. Specific physical properties like electricity conductivity and conductor diameter usually stay constant through the lifetime of the conductors. Conductor emissivity and absorptivity change overtime due to the particulate precipitation during the energization of the line. Conductor electrical current depends on the power system generation and loading.

To accurately model the heat transfer model of a transmission line under the influence of a fire event, assumptions need to be made depending on which thermal case is most fitted in what is studied. There are three main cases that can be considered: the steady-state case, the transient case, and the dynamic case[24]. The steady-state case is when conductor current, conductor temperature, and weather conditions stay the same. The transient scenario assumes the weather conditions are held constant while the conductor electrical current step changes from an initial value to a final value. Under transient case, conductor temperature may not remain constant. Under the dynamic scenario, neither the weather conditions nor electrical current stays

the same overtime. This paper focuses on the transient case due to the nature of a wildfire event and how rapidly it can reach a power line and spread. Hence, weather conditions should remain constant within a very short time after a fire is sparked.

In determining the change of a power line temperature in wildfire events, the net heat transfer calculations are significant. One of the main assumptions in the calculation is that the ACSR conductors may not be isothermal under very high current densities. Heat transfer is the "transport of heat energy from one point to another caused by a temperature difference between those points", as defined in the NFPA 921 Standards. There are a few main modes of heat transfer: magnetic heating, joule heating, solar radiation, convection, and thermal radiation.

Combining the energy of heat transfer from these mechanisms gives the net exchange of energy as follows:

$$Q_{total} = Q_m + Q_c + Q_j + Q_s \pm Q_{conv} + Q_r + Q_w \tag{3.2}$$

where Q_{total} is the net heat transfer energy, Q_m is magnetic heating, Q_c is corona heating, Q_j is joule heating, Q_s is solar radiation, Q_{conv} is natural convective radiation, and Q_r is thermal radiation, and Q_w is wind cooling.

3.3.1 Magnetic Heating

Magnetic heating happens in ACSR conductors and consists of two main types of magnetic heating. Q_{core} is the heat transfer due to the axial alternating magnetic flux generated in the steel core and Q_{tr} is the heat transfer caused by the redistribution of the current densities in the layers of non-ferrous wires. In this study, magnetic heat gain is not considered for the simplicity of calculations.

$$Q_m = Q_{core} + Q_{tr} \tag{3.3}$$

3.3.2 Corona Heating

Corona heating is caused by ionization of air near the conductor. The rate of Corona heating depends largely on surface voltage gradient, which is influenced by atmospheric precipitation. However, high precipitation also results in increased cooling effects, therefore, Corona heating is neglected in the study.

3.3.3 Joule Heating

A conductor that connects to an operating power system heats up from the resistive losses caused by current flow; this process is called joule heating. Some of the key factors which contribute to the current radiation energy are the DC resistance of composite conductors like steel reinforced conductors, the distribution of current density, skin effect, and temperature coefficients. Joule heating for steel core conductors can be calculated through the following equation:

$$Q_j = I_{ac}^2 k_{sk} R_{dc}(1 + \alpha_R(T_c - T_a)) \tag{3.4}$$

where k_{sk} is the skin effect and iron loss factor, which is usually less than 1.02 for conductor sizes of 45mm or less. In the study, a factor of 1.01 is used.

3.3.4 Solar Heating

A bare overhead conductor also receives heat energy from the sun, at a rate that is dependent on the solar angle, the conductor's orientation, the surface condition of the conductor, and so on. For precise calculation of solar heating, numerous parameters need to be taken into account. For example, the power line temperature can be affected by the conductor's inclination to horizontal or the intensity of the direct and diffuse solar radiation. In this paper, only global solar radiation is included in the methodology. The solar heat gain per unit length is determined from effective solar radiation I_t, the absorptivity of the conductor surface α_s, and the outer diameter of the conductor (m). α_s varies from 0.2 to 0.9 depending on the rate of weathering.

$$Q_s = D \times \alpha_s \times I_t \tag{3.5}$$

The global radiation intensity can be calculated from the following equation:

$$I_t = I_b(\sin(\eta) + \frac{\pi F \sin(H_s)}{2}) + I_d(1 + \frac{\pi F}{2}) \tag{3.6}$$

The effective solar radiation depends on multiple parameters. I_b is the direct solar radiation at sea level. F is the incident radiation reflected from albedo or ground. I_d is the diffuse sky radiation to a horizontal surface. H_s is solar altitude in degrees. η is the angle of solar beam with respect to the axis of the conductor in degrees.

The solar beam angle with respect to the conductor axis depends on the solar

altitude, the azimuth of the conductor (γ_c) and of the sun (γ_s).

$$\eta = \arcsin(\cos(H_s)\cos(\gamma_s - \gamma_c)) \tag{3.7}$$

The azimuth of the sun is then calculated from solar altitude, second angle of the sun (ω), and the sun declination, δ_s.

$$\gamma_s = \arcsin(\frac{\cos\delta_s \sin\omega}{\cos(H_s)}) \tag{3.8}$$

The diffuse sky radiation depends on the direct solar radiation at sea level and solar altitude.

$$I_d = (430.5 - 0.3288 I_b)\sin(H_s) \tag{3.9}$$

The direct solar radiation at sea level is determined from the clearness ratio N_s, which ranges from 0.8 to 1.2 depending on the atmosphere, and altitude.

$$I_b = \frac{1280 N_s \sin(H_s)}{\sin(H_s) + 0.314} \tag{3.10}$$

Solar altitude calculation depends on latitude, declination, and second angle of the sun.

$$H_s = \arcsin(\sin\phi \sin((\delta_s)) + \cos\phi\cos(\delta_s)\cos\omega) \tag{3.11}$$

Declination of the sun can be calculated from the day of year based on Julian calendar.

$$\delta_s = 23.3\sin(\frac{2\pi(284+N)}{365}) \tag{3.12}$$

Solar second angle is then calculated using time of the day in seconds.

$$\omega = 0.00416 \times (43200 - t) \tag{3.13}$$

3.3.5 Convection

High conductor surface temperature results in heating of air adjacent to the conductor. There are two scenarios of convective heat transfer. Natural convection occurs when there is no wind speed and heated air rises lead to natural air mass flow. Forced convection occurs when heated air is carried away by the forced air mass flow due to wind or other factors.

Forced convective cooling is considered with different wind speed and the heat loss rate can be determined with IEEE 738 standard. The first equation calculates the heat loss from forced convection at low wind speeds and the second equation give the heat loss resulted from forced convection at high wind speeds.

$$Q_{c1} = [1.01 + 0.0372(N_{Re})^{0.52}]k_f K_{angle}(T_c - Ta) \tag{3.14}$$

$$Q_{c2} = [0.0119(N_{Re})^{0.6}]k_f K_{angle}(T_c - Ta) \tag{3.15}$$

where N_{Re} is Reynold number that is dependent of wind speed, the dynamic viscosity of air, air density, and conductor diameter. K_{angle} is the wind direction factor, and k_f is the thermal conductivity coefficient.

Equation (3.14) is only accurate for a low Reynolds number and equation (3.15) is accurate for a high Reynolds number. Considering the unpredictability of wind speed during one or multiple wildfire events due to the volatile behavior of fire in addition to the environment, the simulation model determines the greater convection loss rate calculated from the two equations.

$$N_{Re} = \frac{D\rho_f V_w}{\mu_f} \tag{3.16}$$

where V_w is the wind speed in m/s, μ_f is the dynamic viscosity of air, ρ_f is the air density, and D is the conductor outer diameter.

The wind direction factor is calculated from the angle between the wind direction and the conductor axis.

$$K_{angle} = 1.194 - \cos(\phi) + 0.194\cos(2\phi) + 0.368\sin(2\phi) \tag{3.17}$$

The dynamic viscosity, density, and thermal conductivity of air are dependent of the film temperature of the conductor, which is the average of the air and conductor temperatures.

$$\mu_f = \frac{1.458 \times 10^{-6}(T_f + 273.15)^{1.5}}{Tf + 383.4} \tag{3.18}$$

Air density is calculated as follows:

$$\rho_f = \frac{1.293 - 1.525 \times 10^{-4} H_e + 6.379 \times 10^{-9} H_e^2}{1 + 0.0036 T_f} \tag{3.19}$$

where H_e is the conductor elevation above sea level. In the simulation, He is assumed to be 100 meters.

The temperature of the boundary layer can be calculated by averaging the temperature of conductor surface and the ambient temperature.

$$T_f = \frac{T_c + T_a}{2} \tag{3.20}$$

3.3.6 Radiation

Thermal radiation is the transfer of heat energy from a hotter object or gas to another object or gas through empty space. It occurs without an intervening medium because the energy is transferred by electromagnetic waves. In the event of a wildfire, energy is transmitted from the fire to the bare overhead conductors by radiation at a rate that depends mainly on the difference between the flame fire and the conductor temperature. The conductor temperature is assumed uniform throughout the cross-section of the line. Radiative heat transfer between fire and conductor surfaces can be determined from the following equation:

$$Q_{rad} = A_f \varepsilon \sigma F_{f \to c} [(T_f + 273.15)^4 - (T_c + 273.15)^4] \tag{3.21}$$

where σ is the Stefan-Boltzmann constant ($5.6697 * 10^{-8} W m^{-2} k^{-4}$), and ε is emissivity of 0.8. A_f is the area of fire, T_f is the fire temperature in °C, and T_c is the conductor temperature in °C. $F_{f \to c}$ is the view factor, which is the proportion of the radiation which leaves fire and reaches the conductor surface. The conductor surface temperature in this paper is approximated to be the conductor core temperature for simplicity of calculation.

View factor is needed to calculate the rate of heat transfer by radiation between the flames and power line surface in any direction. It is generally defined as the fraction of radiation leaving a surface which is transferred to another surface directly. The symbol $F_{1 \to 2}$ denotes the view factor leaving surface A_1 and arriving surface A_2. In the heat transfer model, view factor from the fire to the conductor surface is considered. View factors change based on the object's geometry and size, and the orientation and position of the two surfaces. A view factor value is between 0 and 1

and all the view factors of a surface should sum to 1.

$$F_{f\to c} = \frac{1}{A_f}\int_{A_f}\int_{A_c}\frac{cos\Theta_f cos\Theta_c}{\pi s^2}dA_c dA_f \tag{3.22}$$

For simplicity, view factor is calculated with the fire modeled as a sphere as shown in Figure 3.4. The view factor for $\Theta \leq \frac{\pi}{2} - \Phi$ is calculated through equation (3.23).

$$VF = \frac{r^2}{L^2}\cos\Phi \tag{3.23}$$

where r is the fire radius, L is the distance between the center of the fire and the conductor segment center, and Φ is the orientation angle in radian.

The view factor for $\Theta < \frac{\pi}{2} - \Phi$ is calculated through equation (3.24). This equation only applies when the conductor segment only "sees" the fire partially.

$$VF = \frac{1}{2} - \frac{1}{2}\arcsin(\frac{(L^2-1)^{0.5}}{L}) + \frac{\cos(\Theta)\arccos(-(L^2-1)^{0.5})\cot(\Theta)}{\pi L^2} - \frac{(L^2-1)^{0.5}(1-L^2(\cos^2\Theta)^{0.5})}{\pi L^2} \tag{3.24}$$

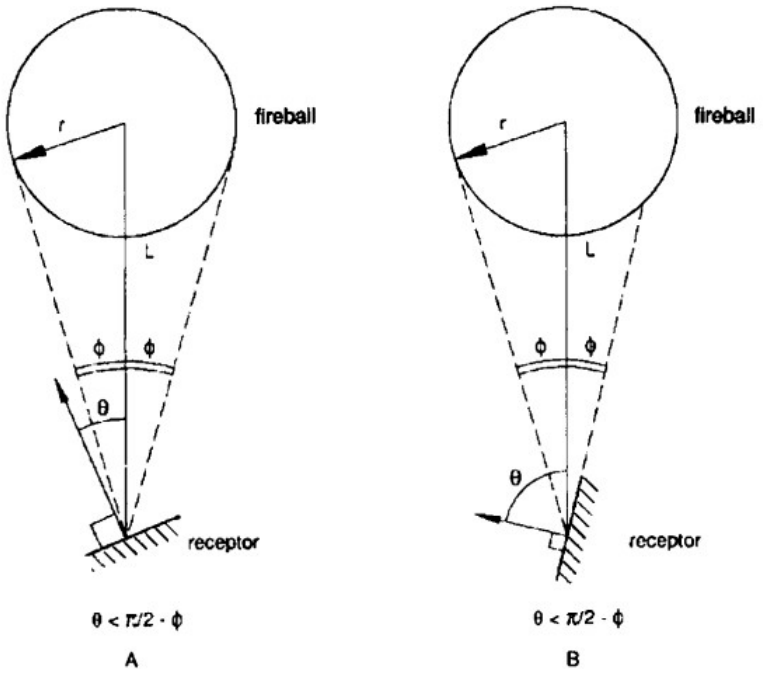

Figure 3.4: View Factor of the Most Affected Transmission Line Segments in the Power System Overtime. These segments are parts of transmission lines TL111, TL112, and TL113.

In the case of fires, only four modes of heat transfer that are considered to contribute the most in the change of conductor temperature. The four main modes are joule heating, solar radiation, convection, and thermal radiation. Combining the energy of heat transfer from these mechanisms gives the net exchange of energy as follows:

$$Q_{total} = Q_j + Q_s + Q_r \pm Q_{conv} \tag{3.25}$$

Given the net heat transfer, the temperature of the object can be determined using the following non-linear ordinary differential equation:

$$\frac{dT}{dt} = \frac{Q_{total}}{mc} \tag{3.26}$$

where m is the mass of the object in grams, and c is a constant representing the heat capacity of the materials.

An ACSR conductor contains mainly aluminum strands and a steel core; the transfer of most of the heat from aluminum strands to the core only takes up to a minute. Hence, the heat capacity of the ACSR conductor can be calculated by adding the heat capacity of aluminum and the heat capacity of steel during a transient case, assuming the temperature is uniform across the conductor.

$$mc = m_a c_a + m_s c_s \tag{3.27}$$

where m_a and ms are the mass per unit length for aluminum and steel. c_a and c_s are the specific heat of aluminum and steel. The masses per unit length used for aluminum and steel are $897\frac{kg}{m}$ and $481\frac{kg}{m}$. The specific heat of aluminum is assumed to be $1.116\frac{J}{kgK}$ and the specific heat of steel is $0.5119\frac{J}{kgK}$.

3.4 Line Sag Calculations

As the transmission line is heated it also expands and incurs an expansion in the line length. The equation for line expansion is shown as below:

$$\Delta L = \alpha L \Delta T \tag{3.28}$$

where L is the length of the wire, ΔT is the change temperature, and α is the coefficient of linear expansion for Aluminum Conductor Steel Reinforced (ACSR) wire, which is the material commonly used for transmission lines [46].

Coefficient of thermal elongation (CTE) depends on the ratio of aluminum to steel

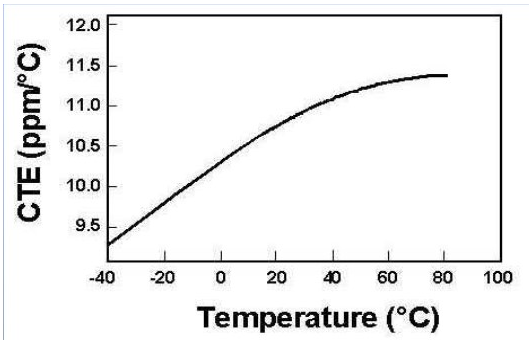

Figure 3.5: Change in Coefficient of Thermal Elongation of a Typical Steel Material.

for ACSR conductors. Aluminum tends to expand twice as fast as steel and hence it has a larger coefficient of thermal elongation. The CTE of an ACSR conductor does not stay constant as it changes with the change in conductor temperature. A typical CTE curve for a steel material is shown in Figure 3.5 [9]. Because the CTE of aluminum expands at a faster rate than steel, the CTE of an ACSR conductor is estimated based on the CTE pattern over temperature for a typical aluminum material [2] [3]. The CTE of the ACSR starts at $18.9 * 10^{-6} \frac{1}{^\circ C}$ at 20 $^\circ C$. From the curve shown and the typical CTE of aluminum, the CTE estimation is linearly approximated and is shown and applied in the simulation in section 4.

As the transmission line expands, it also tends to sag, or sink down from the horizontal level between the towers. The calculation of line sag is based on a catenary equation of the line segment between towers. In Figure 3.6, x represents horizontal distance from the minimum to a point of the catenary, y(x) is the vertical distance from the minimum to the same point. H is the horizontal component of tension in Newton and w is the weight per unit length in N/m.

The line sag calculation is an approximation of a parabolic equation based on the first term of the MacLaurin expression of the hyperbolic cosine, which is valid when $\frac{x^2 w^2}{12H^2}$ is much less than unity. The sag calculation can be simplified to equation (3.30) by substituting sag with 2x in equation (3.29).

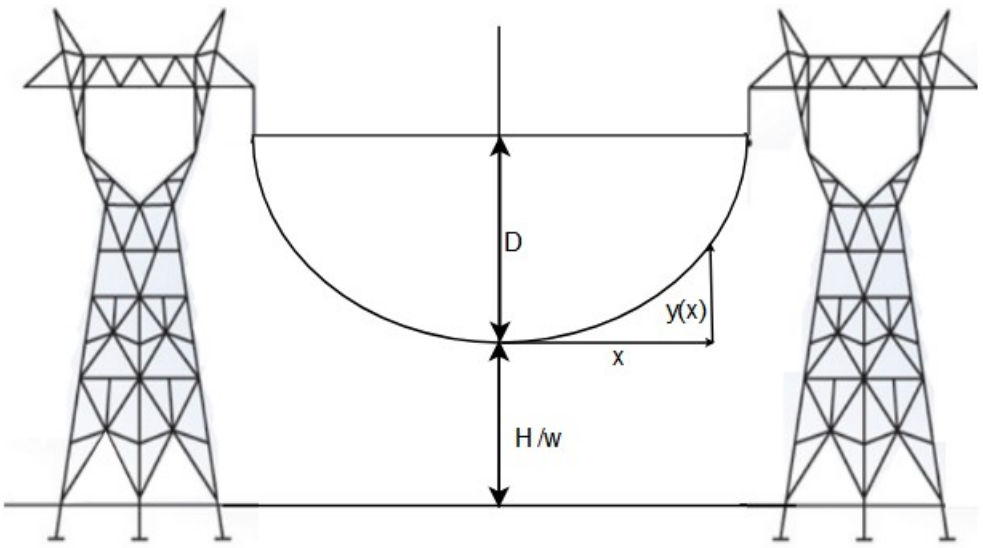

Figure 3.6: Overview of heating dynamics from wildfire to power infrastructure via radiation, conduction, and convection.

$$D = \frac{H}{\omega}[\cosh(\frac{\omega S}{2H}) - 1] \tag{3.29}$$

$$D = \frac{\omega S^2}{8H} \tag{3.30}$$

The power line segment length between towers can be calculated through equation (3.31) based on the catenary curve of the line sag, which can be approximated to equation (3.32).

$$L = \frac{H}{w}\sinh(\frac{wx}{H}) \tag{3.31}$$

$$L = x(1 + \frac{w^2x^2}{6H^2}) \tag{3.32}$$

The equation can also be simplified by substituting sag D with 2x. The sag can then be calculated from the simplified equation (equation (3.34)).

$$L = S + \frac{8D^2}{3S} \tag{3.33}$$

$$D = \sqrt{\frac{3 \times S \times (L - S)}{8}} \tag{3.34}$$

where S is the span length of the line between two towers, and L is the line length between the towers, which is the sum of the span length and the slack.

Slack can then be calculated from deriving the above equation:

$$\Delta L = \frac{w^2 l^3}{24H^2} \tag{3.35}$$

During thermal elongation, the conductor length between towers increases while the span length stays unchanging, which causes the conductor tension to decrease. Therefore, the effects of strain under tension also need to be considered for calculating sag when the conductor is overheating. The cable length at a certain temperature can be calculated through equation (3.36) [57].

$$L = L_o(1 + \alpha\Delta T)(1 + \frac{\Delta H}{EA} + \epsilon_c) \tag{3.36}$$

Using polynomial expansion and equating the equation to equation (3.35), final tension H_f can be calculated by rearranging the polynomial and equating it to zero. It becomes a cubic equation with the following constant coefficients (from higher to lower order):

$$
\begin{aligned}
a_3 &= (\frac{1}{EA})(1 + \frac{w^2 l^2}{24 H_0^2})(1 + \alpha \Delta T) \\
a_2 &= (1 + \frac{w^2 l^2}{24 H_0^2})(1 + \alpha \Delta T)(1 - \frac{H_0}{EA} + \epsilon_c) - 1 \\
a_1 &= 0 \\
a_0 &= \frac{w^2 l^2}{24}
\end{aligned}
\tag{3.37}
$$

where ϵ_c is the permanent elongation of the cable.

Sag correction is considered when the sag exceeds 5% of the span length and added to the sag calculation[7].

$$
Correction = D^2 \frac{w}{6H} \tag{3.38}
$$

where D is line sag, w is conductor unit weight, and H is horizontal tension.

3.5 Integration of a Synthetic Power Grid

An aerial map is created using MATLAB from importing the geographical coordinates of the synthetic substations in Tennessee, which is shown in Figure 3.7. A synthetic electrical network from the Illinois Center for a Smarter Electric Grid (ICSEG) is referenced and used for the simulation [11]. This system contains 150 buses and 217 branches. It has a total generation capacity of 23846 MW. It was modeled with geographic coordinates that correspond to a geographical representation of Tennessee, as well as other parameters to emulate a simple, realistic power system. The red triangle symbol on the map represents a randomly generated fire.

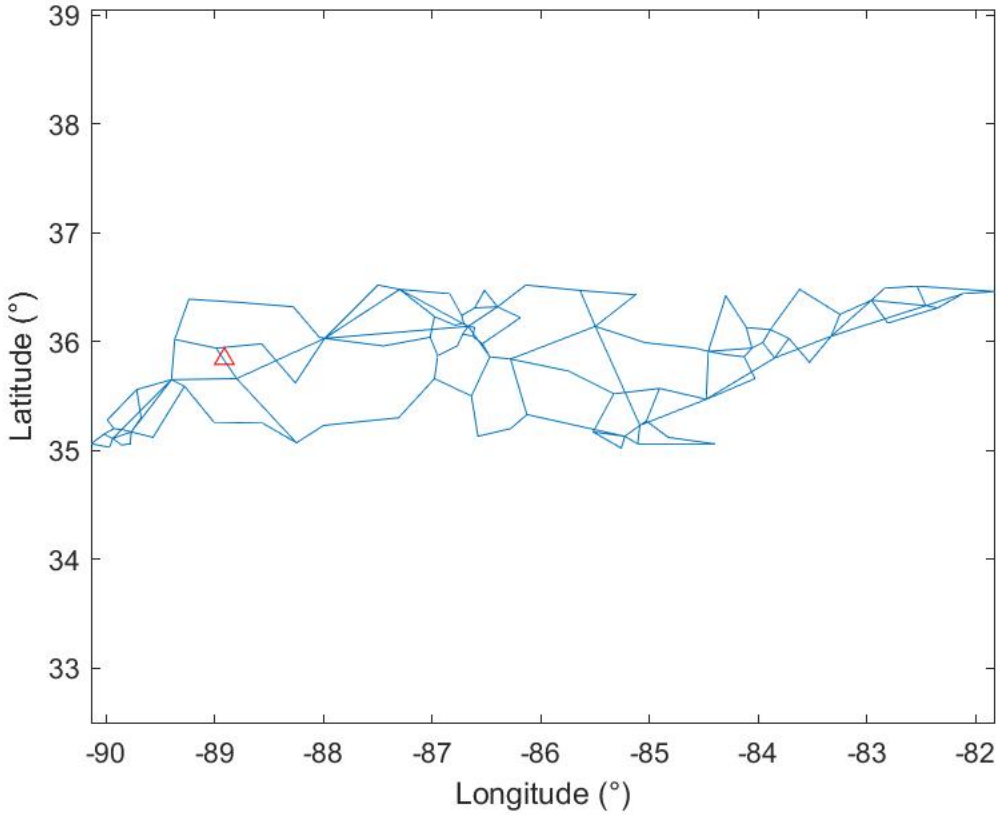

Figure 3.7: Aerial Map of the 150-Bus Synthetic Grid on Footprint of Tennessee.

3.6 Load Flow Analysis

In this paper, steady-state power flow simulations are performed in order to determine the current through transmission line, which is highly correlated to the change in conductor temperature during a fire event. The following formula is used to calculate power factor:

$$pf = \frac{P}{\sqrt{P^2 + Q^2}} \tag{3.39}$$

where pf is power factor, P is real power transferred in kW and Q is reactive power in kVAR.

Then the calculated power factor is used to determine the current through the powerline as the following equation. The equation is then used for calculating the current heating of the conductors.

$$I = \frac{P}{\sqrt{3} \times pf \times V} \tag{3.40}$$

where I is the current through the transmission line, and V is line-to-line voltage.

Load flow analysis is performed using MATPOWER, an open-source power system simulation tool that can be run within MATLAB. From the steady-state simulation, necessary AC power parameters are calculated from the bus and branch voltages, real power, and reactive power. There are some of the main assumptions in this paper:

- The simulation does not consider elevations of a geographic location nor the effects of them on fire expansion speed.
- The absorptivity for solar heating is assumed to be constant.
- The conductor size is assumed to be the same for all power lines.
- Only perpendicular wind direction to the conductor is considered in this simulation.
- All the lines have the same absorptivity and emissivity.
- Each transmission line is evenly divided to the same span length along the line based on an ideal span length of 300 meters.
- The electric power network used only considers fire impact on the transmission system of the utility.

Chapter 4

SIMULATION RESULTS AND DISCUSSION

In this section, a detection algorithm using a 150-bus power system test case is created and the model is simulated. The results of simulation are then analyzed in this section.

4.1 Simulation Results and Analysis

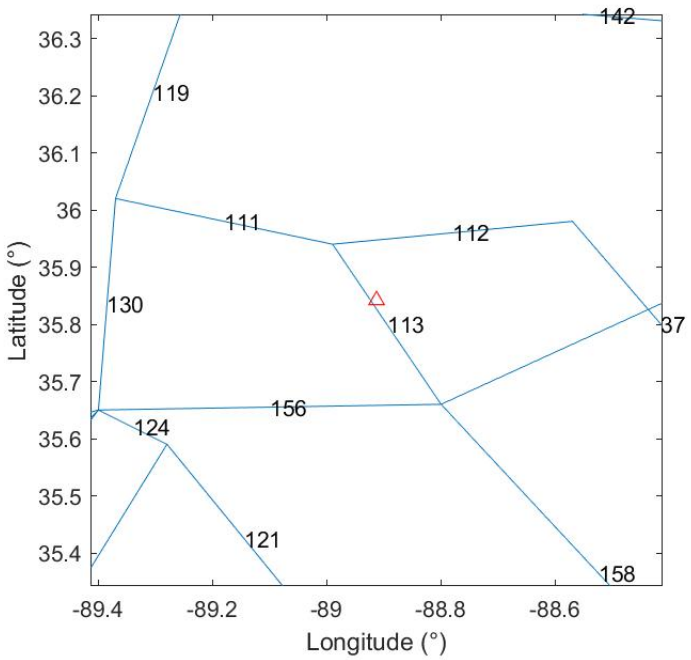

Figure 4.1: Randomly Generated Fire Location on the Synthetic Grid of Tennessee with Transmission Lines Labeled.

Figure 4.1 shows a zoomed-in portion of the aerial map around the fire location (the triangle symbol represents fire), which is generated using MATLAB. The transmission lines are labeled in numbers for easy reference only. From the aerial map, the

fire location is generated close to the center of power line TL113. The further lines to the fire are TL112 and TL111. The fire is created radially within a limit to the center of the smaller line segments. The limit is 0.01 degrees in longitude and 0.01 degrees in latitude from any randomly chosen line segment. 0.01 degrees change in longitude corresponds to 1.11 km and 0.01 degrees change in latitude equates to approximately 0.91 km. The simulation considers the results from three transmission lines that are closest to the fire.

The proposed algorithm can help identify the specific transmission lines most impacted by the fire. It also allows us to pinpoint the exact span segments of the lines closest to the fire, which are segment 46 of TL113, segment 24 of TL112, and segment 141 of TL111. The segment number increases from higher latitude, lower longitude to lower latitude and higher longitude, which agrees with the fire location relative to the lines in Figure 3.7.

After integrating the power grid and performing load flow analysis, a heat transfer model is created to calculate the net heat transferred to the power lines. The heat transfer algorithm includes joule heating of the energized ACSR conductors, thermal radiation from the fire, solar heating, and forced convection. It also uses random realistic weather data like air temperature (between 20 $^{\circ}C$ and 37 $^{\circ}C$), clearness ratio (between 0 and 1.2), and random day of the year. The simulation algorithm assumes a fire event that occurs at 9 o'clock in the morning.

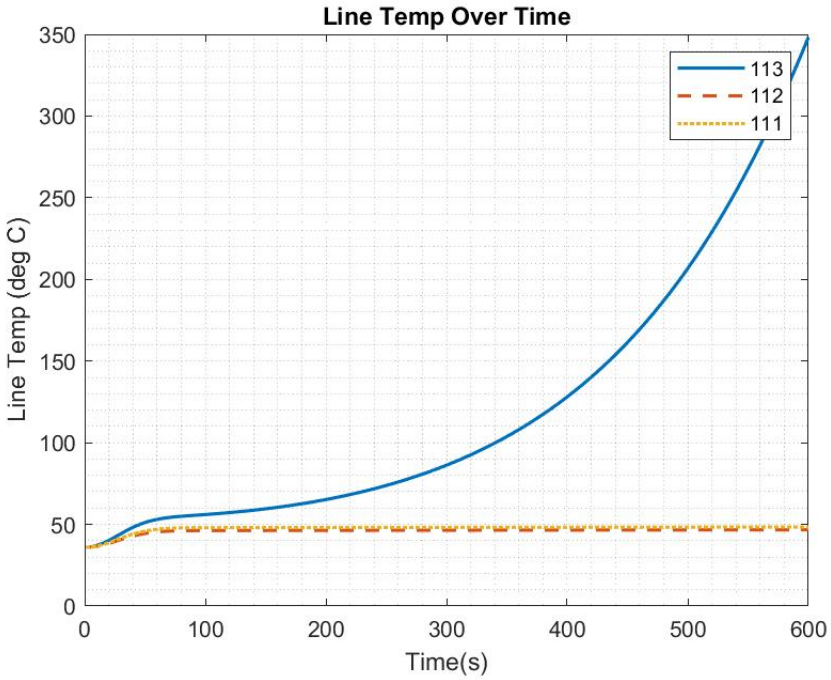

Figure 4.2: Line Temperature Over Time for the Three Most Affected Transmission Line Segments in the Power System. These segments are parts of transmission lines TL111, TL112, and TL113.

As a result, Figure 4.2 shows the conductor temperature along the closest line segments to the fire, which are parts of transmission lines TL111, TL112, and TL113. This figure is created using MATLAB. With the assumption that the weather parameters are constant within one simulation trial, and there is a step change in the electrical current from t = 0, the conductor temperature increases gradually after t = 0 at a rate from Equation (3.26). A significant difference is that while the temperatures in line segments from TL112 and TL111 reach steady state after 75 seconds, the line segment temperature from TL113 continues to rise and it begins to rise exponentially. This is the segment most affected by the fire because the initial distance between the fire and the conductor is approximately 836.3 meters. As fire expands and moves closer to the line, its radiative heating increases exponentially over time and hence contributes significantly to the total heat transfer. The distances from the fire to the other segments are both over 10 kilometers. Therefore, they are not really

affected much by the fire event.

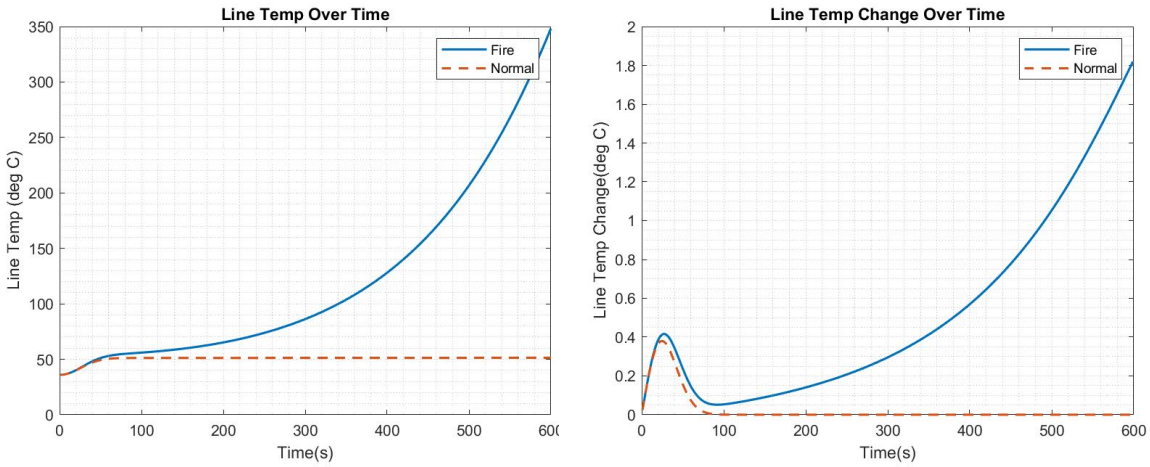

(a) From t = 0 to t = 600s (b) From t = 0 to t = 100s

Figure 4.3: Line Temperature and Temperature Change Over Time for TL113

Generated using MATLAB, the temperature curves of the power line TL113, span segment 46 over the simulation duration of 600 seconds under a fire event and a normal situation are shown in Figure 4.3a. The secondary y-axis on the right side of the graph corresponds to the conductor temperature under normal conditions, meaning no potential fire hazards. The line temperature under a fire event changes significantly as compared to the temperature without any fire hazard. Because this line segment is the closest to the fire location, the rate of temperature change is dominated by the fire rate of spread. Under normal conditions, the conductor temperature increases exponentially until it reaches 75 seconds. The rate of conductor temperature change then slows significantly; the temperature characteristics curve becomes linear after 120 seconds as it reaches steady state. The thermal time constant of the temperature curve under normal condition is 32.5 seconds. The "settling time" is at 61 seconds when the line temperature is within 2% of the steady-state value.

From observing the curves in Figure 4.3b within 100 seconds, the line temperature starts increasing gradually because of the step change from the initial electrical current

at t = 0. After about 25 seconds, the temperature change is reduced due to the exponential increase of the wind cooling. The temperature profiles of both scenarios have the same characteristics until it reaches 100 seconds. After 100 seconds, the line temperature rate increases exponentially under fire influence while the conductor temperature rate remains constant in the normal case.

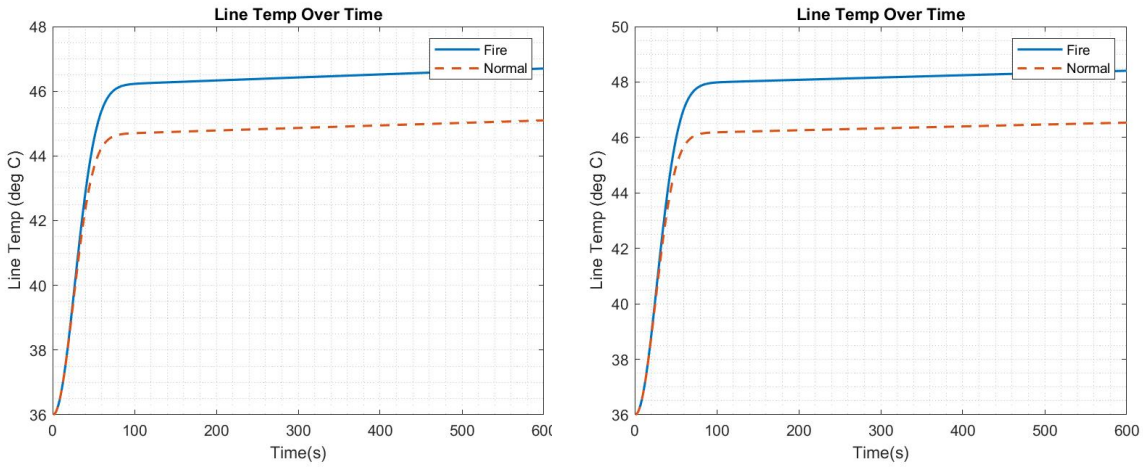

(a) TL112 (b) TL111

Figure 4.4: Line Temperature Over Time for TL111 and TL112

Figure 4.4 shows the conductor temperature curves of line segments of TL111 and TL112 under both normal and fire scenarios created and simulated using MATLAB. The graphs indicate that under fire influence, both line temperatures increase with the same characteristics as under normal condition. At the time when the line temperatures start to settle and reach steady-state values in the normal case, the fire impacted conductor temperatures continue to rise until around 100 seconds. Neither of the temperatures increase like that of TL113 because both line segments are over 11 km away from the fire center; therefore, they are not as impacted. The temperature of TL111 rises to a higher value than that of TL112 because of the different angles between the fire and the lines. As shown in Figures 4.1 and 3.4, the segment of TL112 "sees" the fire while that of TL111 does not "see" the fire entirely as fire expands overtime. Complete visibility of fire to the line segments affects the view

factor calculation, and hence the energy transferred by thermal radiation. This in term causes the differences of the final temperature values.

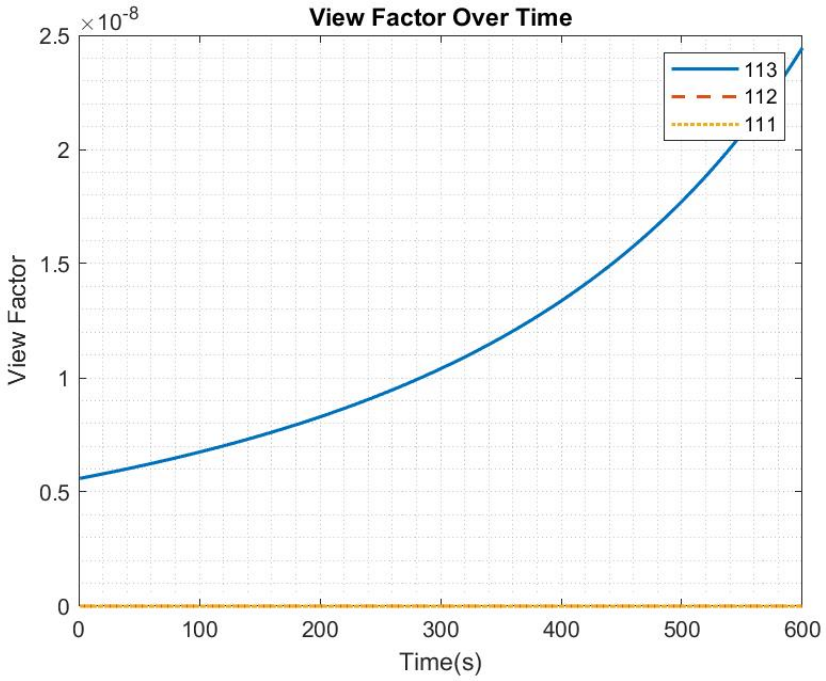

Figure 4.5: View Factor of the Most Affected Transmission Line Segments in the Power System Overtime. These segments are parts of transmission lines TL111, TL112, and TL113.

View factor characteristics of the power line segments are shown in Figure 4.5, which are created and simulated using MATLAB. The view factor for the further power lines does increase over time but in much smaller increments compared to the view factor change in TL113. The view factor of TL113 increases exponentially as the fire area expands exponentially. The view factors of the other line segments are not affected by the fire as much because they are a lot further away.

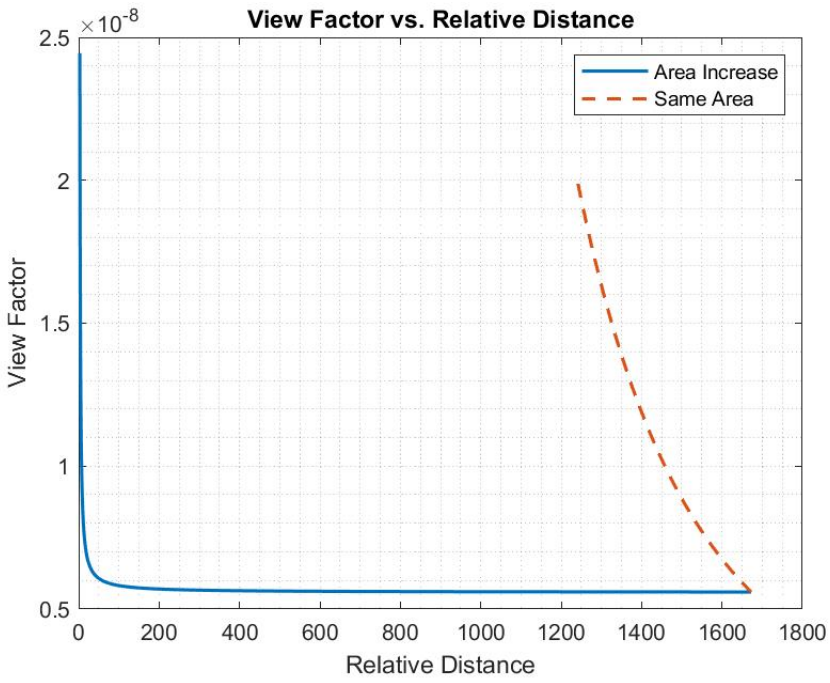

Figure 4.6: View Factor of TL113 Segment 46 as a function of Relative Distance.

Figure 4.6 shows the view factor as a function of relative distance ($\frac{L}{r}$), which are created and simulated using MATLAB. The fire spreads rapidly at a rate of 0.36 m/s, but does not reach the conductor, so the view factor does not reach 1 at the end of the simulation. The dashed line on the graph is the view factor as a function of relative distance in the case that the fire area remains the same while the fire moves at the same speed. This scenario can happen when there are light fuels, and the old fuels get burned out quickly as the newer fuels are ignited. The view factor only goes up to 1.98^{-8} as compared to the 2.43^{-8} view factor with increased area at the end of simulation.

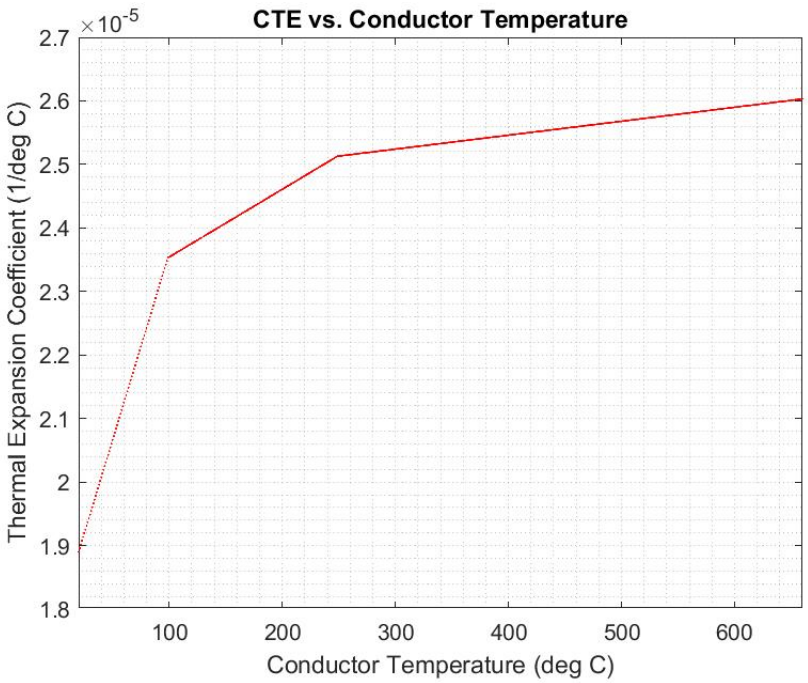

Figure 4.7: Coefficient of Thermal Elongation of the ACSR Conductor Curve.

The coefficient of thermal elongation (CTE) of the ACSR conductor is estimated and shown in Figure 4.7, which are created and simulated using MATLAB. As mentioned in section 3, the coefficient of thermal elongation increases when conductor temperature increases overtime. However, based on Figure 3.5, the CTE increases at slower rates when the conductor reaches certain temperature limits.

Figure 4.8 shows the thermal elongation and sag of the conductor segments closest to the fire over time, which are created and simulated using MATLAB. The sag characteristics of the line segments follow mostly the expansion curves. Figure 4.8c shows the change in line sag of the most affected power line segment (TL113, segment 46) over time. This figure compares the results for two different scenarios in the same line segment. The solid, blue line represents the scenario under a fire event and the dashed, orange line represents the scenario without any fire. It indicates that the line sag increases gradually from t = 0 due to the step change from the initial current in

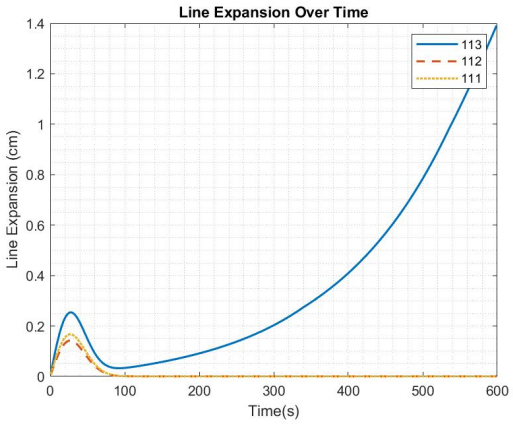

(a) Line Expansion Over Time

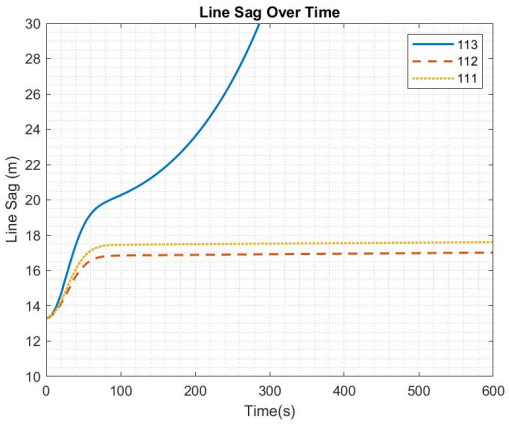

(b) Line Sag Over Time

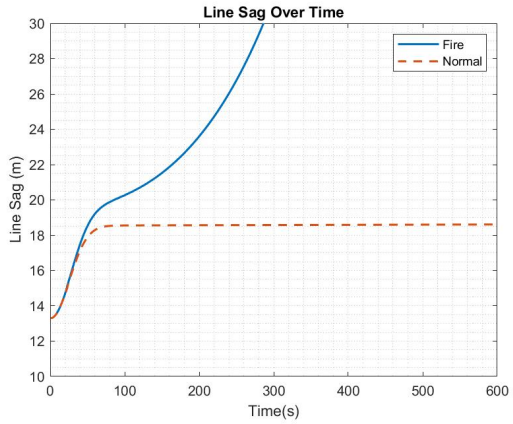

(c) Line Sag Comparisons of Normal and Fire Simulations for TL113

Figure 4.8: Line Expansion and Line Sag Over Time

the algorithm. Under normal conditions, the line sag reaches steady state after 75 seconds. Meanwhile, the line sag continues to rise exponentially under a fire event. The "settling time" is at 61 seconds when the line sag is within 2% of the final value. The difference in sag between these scenarios is about 3 meters at 150 seconds. From the result comparison in Figure 4.8c, a fire can be detected early within 150 seconds as the line sag deviates from its expected value under normal condition.

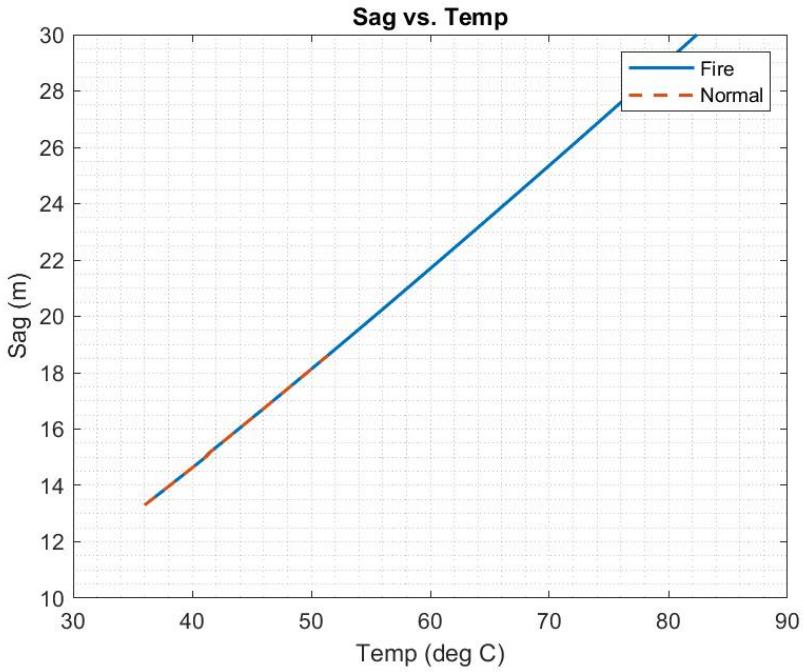

Figure 4.9: Sag and Conductor Temperature Relationships for TL113

Figure 4.9 shows the line sag against the conductor temperature of the most affected power line segment (TL113, segment 46), which are created and simulated using MATLAB. This figure compares the results for two different scenarios. The thinner, blue line represents the scenario under a fire event and the thicker, orange line represents the scenario without any fire. With the same heat transfer parameter values and weather and time data, the figure shows that the line sag is directly proportional to the conductor temperature.

This paper references a new type of smart sensor Ampacimon to analyze the accuracy and capability of line sag sensors in detecting early wildfires. An Ampacimon sag sensor operates with a conductor temperature range of between -40 °C and 200 °C [4]. Beyond this range, the sensor is either damaged or fails to take accurate measurements. Accuracy in measuring line sag is an important factor in fire events. Hence, the temperature threshold needs to be considered in the simulation. From the

results in Figure 4.2, the line temp of TL113 segment reaches 200 °C at around 468 seconds. Therefore, only results before that time should be considered as the sensor may not function properly with high heat. There needs to be a solution that will help increase the temperature threshold.

The Ampacimon sensor is most accurate in taking real-time line sags measurements when they are under 25 meters, which is reached after 225 seconds as shown in Figure 4.8b under fire influence for TL 113 [26]. Within this sag threshold, the error margin of measurement of the sensor is no greater than 20 cm, but this is mainly important in predicting the ampacity of the line. In terms of early wildfire detection, detection time is more important. If the change in line sag is tracked in real-time, a potential fire hazard within 1 km distance from the line can be detected with the assumption that the sag will exceed the maximum sag limit of 25 meters. The detection standard can change based on factors like the accuracy of the sensors, maximum permissible clearances from ground, and line span.

4.2 More Observations and Discussion

4.2.1 Fire-Resistant Material and FEMM Modelling

In order to protect the line sensors and ensure they do accurate measurements, fireproof materials like silica fabrics should be utilized so that the sensor is protected from intense radiant heat. silica fabrics are a type of fine woven silica fiber cloth that is made of sodium silicate. Because of the physical and thermal properties of sodium silicate, silica fibers can withstand up to 1000 °C for a long period of time and up to 1700 °C for a transient case [60]. In contrast, the Aluminum melting point of 660.32 °C [36]. Hence, the utilization of silica fabrics on the sensors can help withstand heat for a longer period as the fire spreads towards the line.

There are various ways of producing sodium silicate. It can be obtained by mixing silica, sodium hydroxide, and water. It can also be produced through dissolving silica in sodium carbonate. The preparation process is simple and does not require many complex steps.

Besides the simplicity of silica fabrics manufacturing, an advantage to using silica fabrics for fire protection is that there is an abundance in the raw materials that are needed in the manufacturing process.

Since the Ampacimon sensor harvests energy from a current transformer (CT), external electromagnetic fields can affect its accuracy in measuring sag[39]. The block diagrams of the sensor can be seen in Appendix C. Anything near an operating sensor should not have impacts on the magnetic field because the alternating current that powers the sensor is induced from the alternating magnetic field in the core of the CT. Therefore, a FEMM model needs to be created and simulated to determine whether the chosen fire-resistant material affects the magnetic field of the circuit.

Sodium silicate has an electrical resistivity that increases with temperature, but still large in value based on the resistivity of silicon dioxide at various temperatures and the inability to conduct electricity of sodium oxide. [33][35]. Hence, its electrical conductivity is 0. It is also non-magnetic, so its relative permeability is approximately 1 regardless of the relative densities [30]. Therefore, adding the silica fabrics on the line sensors should not affect the circuitry or operation of the sensors.

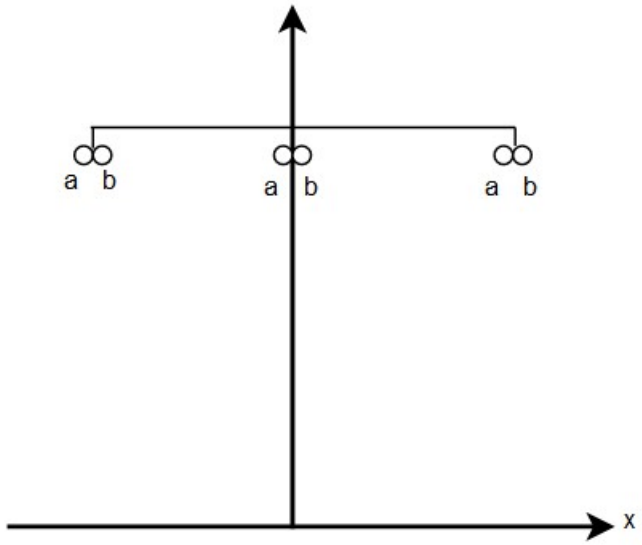

Figure 4.10: Cross Section of an Overhead Power Line

Figure 4.10 shows the cross section of an overhead transmission line, which is drawn using draw.io. The model is created as shown in Figure 4.10, which is composed of two subconductors per phase. The magnetic field generated from the cross section of the power line is simulated and observed from left to right along the x coordinate. The graph in Figure 4.11 illustrates the magnetic field distribution of the overhead line, which is a result from simulating the model of the transmission lines in FEMM. FEMM is an open-source software which allows users to solve electromagnetic problems. The curve indicates that most of the observed magnetic fields are clustered near the center and start to decline further away from the center.

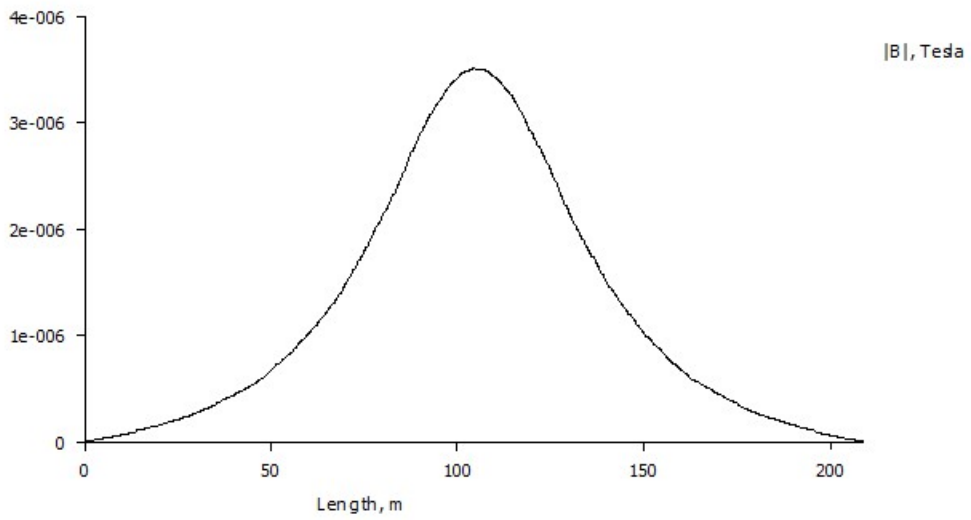

Figure 4.11: Magnetic Field Curve with the Coordinate x (from left to right)

The electrical resistivity of Silica fibers decreases with increased temperature based on the properties of silicon dioxide and sodium oxide. Assuming the fire temperature gets to over 1000 $°C$, the resistivity of the material can reach about 4600 Ωm, which gives an electrical conductivity of $2.174 * 10^{-10} \frac{MS}{m}$. The magnetic field values are plotted using Excel and shown in Figure 4.12. The plot includes the magnetic fields produced by the transmission lines before and after silica fabrics are applied on the sensors and the difference between them. The magnetic field differences are so small that they can be neglected, based on the results shown in Figure 4.12. Therefore, silica fabrics can be a good add-on to the line sensors and should not affect the operation of the sensors while providing thermal protection.

Silica fibers have the reputation in its fire protection applications such as the manufacturing of plastic pipe fire stop devices, as well as thermal insulation for engines, compensators, and other electrical equipment. Braided silica sleeves are also utilized to protect pipes and hoses from extreme high heat. To say the least, the history of silica fabrics applications has proven that they are highly reliable in protecting the line sensors from a fire event.

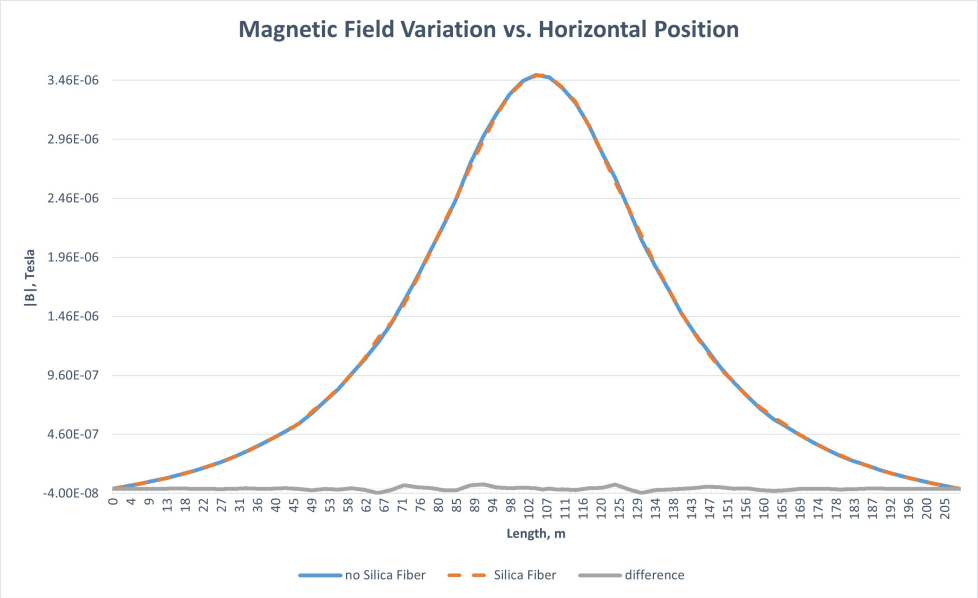

Figure 4.12: Magnetic Field Curve with the Coordinate x (from left to right)

Due to the abundance in materials and simplicity in the manufacturing process, the cost of silica fibers is affordable and relatively cheaper than most other fire-resistant materials.

4.2.2 Dynamics of Wind

In this subsection, the limitations of line temperature and sag threshold of the line sensors are not considered as the focus is to study how the dynamics of wind movement affects wildfire rate of spread, and hence the line sag.

Wildfire expansion rate highly depends on the wind speed; hence their relationship needs to be taken into account when estimating fire behavior. In the simulation, crown fire rate of spread (ROS) is considered; it is the spread rate of wind-driven, active crown fire. BehavePlus 5.0.5, a popular fire modeling software is then used to determine the crown fire ROS and the connection between wind speed and fire rate of expansion more realistically.

Crown fire ROS is determined from a correlation using the Rothermel's surface fire spread model and only two variables are needed [52][53]. The variables are the 20-ft wind speed and the surface fuel moisture levels (1-h, 10-h, 100-h, and live woody moisture). In general, a 20-ft wind speed is measured 20 feet above the trees for crown fires in the United States. The 1-h, 10-h, and 100-h moisture levels are the dead fuel moisture measured in different time lags while live woody moisture is the moisture content of dry plant material in shrubs. The calculation is run with the assumption that a fire happens in a dry area and spot fires are possible, so the 1-h, 10-h, and 100-h moisture levels are chosen to be 4%, 5%, and 6% [8][5]. The live woody moisture values are selected from 40% to 100%, with 20% increment. As a result, the crown ROS curves with different wind speeds and live woody moisture levels is shown in Figure 4.13, which is simulated and plotted using BehavePlus using the selected variables. As the 20-ft wind speed increases, the crown fire ROS also increases. In addition, more live woody moisture levels reduce the crown fire expansion rate. In other words, more severe fire conditions lead the wildfire the spread more rapidly.

Figure 4.13: Crown Rate of Spread as a Function of 20-ft Wind Speed (Upslope).

The 20-ft wind speeds and crown fire rates of spread with 40% live woody moisture are used as inputs for the algorithm as worst-case scenarios. Table 1 shows the simulated scenarios with different wind speeds and the related fire ROS. The fire location also remains the same for these scenarios. The wind direction also maintains perpendicular to the power line and only the impacts of the wind speeds are analyzed.

Figure 4.14 shows the TL113 line sag curves over time with 5 different wind speeds, which is generated using MATLAB. It is simulated using the 20-ft wind speeds and fire rates of spreads resulted from BehavePlus. It is apparent that the line sag increases the most with lower wind speeds, but there are other factors that contribute to the change in line sag. The increase of wind speed causes the fire ROS to increase but at the same time it reduces the convective heat loss as the fire has not reached the line. As the fire moves more rapidly towards the line, the heat transferred to the line increases exponentially even when it has not reached the line. Convective heat

gain from the fire is not considered here. The zoomed-in portion of the sag curves for higher wind speeds are shown on the right of the graph.

Table 1: Inputs for the Simulation with Different 20-ft Wind Speeds and Crown Fire Rate of Spread.

Wind Speed (m/s)	Fire ROS (m/s)	Wind Angle (deg)
0	0.03	90
1.4	0.06	90
2.8	0.12	90
4.2	0.20	90
5.6	0.29	90

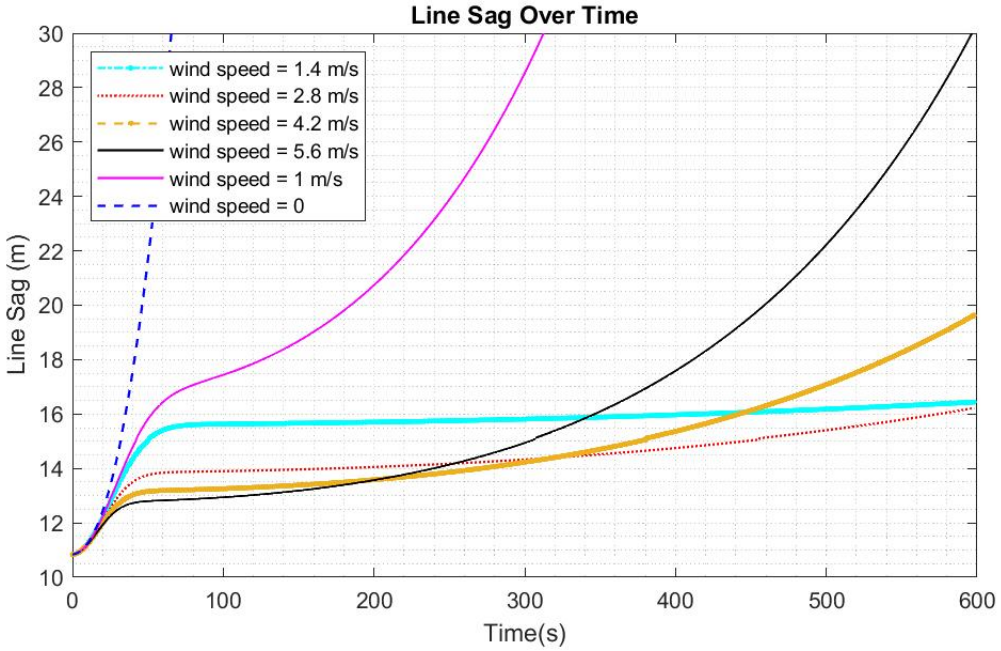

Figure 4.14: Line Sag Over Time with Four Different Wind Speeds.

Table 2 shows simulated scenarios with different wind angles with respect to the closest power line. The wind speed, fire ROS, and fire location are held the same for these scenarios. Figure 4.15 shows the line sag curves over time with the four different wind angles with respect to the power line TL113. It is generated using MATLAB with the highest wind speed and fire rate of spread resulted from BehavePlus. The wind speed stays at 5.6 m/s and the fire rate of spread is held at 0.29 m/s The sag curves indicate that the final line sag increases with the decrease in wind angle.

Table 2: Inputs for the Simulation with Different Wind Angles With Respect to the Power Lines.

Wind Speed (m/s)	Fire ROS (m/s)	Wind Angle (deg)
5.6	0.29	0
5.6	0.29	30
5.6	0.29	45
5.6	0.29	60
5.6	0.29	90

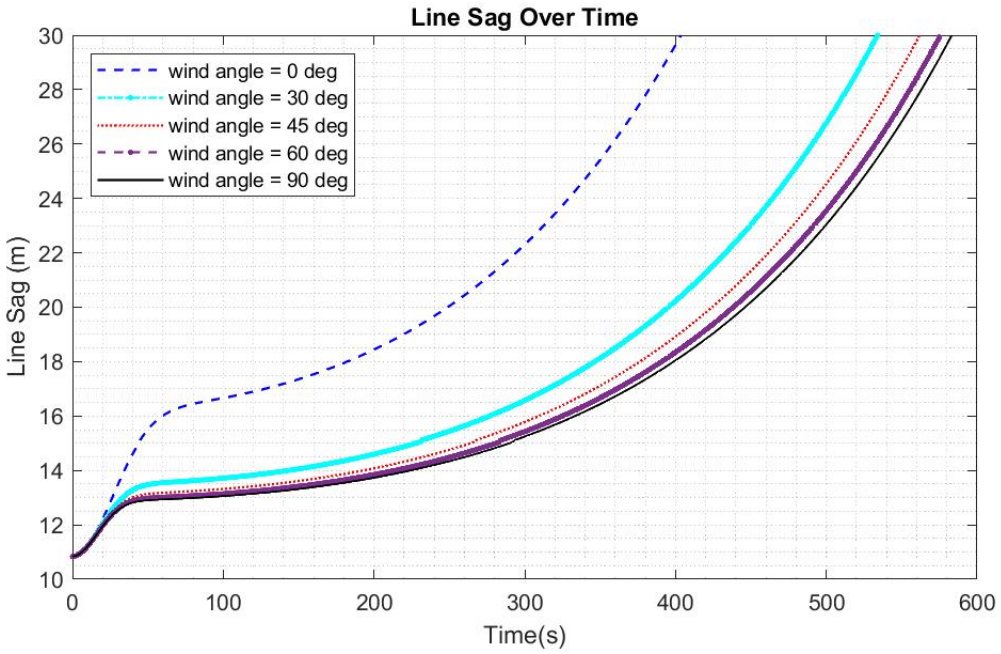

Figure 4.15: Line Sag Over Time with Four Different Wind Angles With Respect to the Line Segment.

4.2.3 Additional Scenarios with Different Cutoff Distances

In this subsection, the limitations of line temperature and sag threshold of the line sensors are not considered as the main focus is to study how the starting fire locations affect the heat transfer model, and hence the line sag over time.

Table 3 shows the cut off distances and actual distances between the most affected power line segments of TL113 and the fire. It also shows the exact segment that is the closest to the fire. Several simulations run at cut off distances and the results are plotted and analyzed.

Table 3: Inputs for the Simulation with Different Cutoff Distances from the Fire to the Center of Segments.

Cutoff (deg)	Affected Segment	Actual Distance (m)	Does Fire Reach the Line?
0.003	47	270.3	YES
0.005	46	432.7	YES
0.01	46	836.3	NO
0.02	45	1672.6	NO
0.03	43	2506	NO

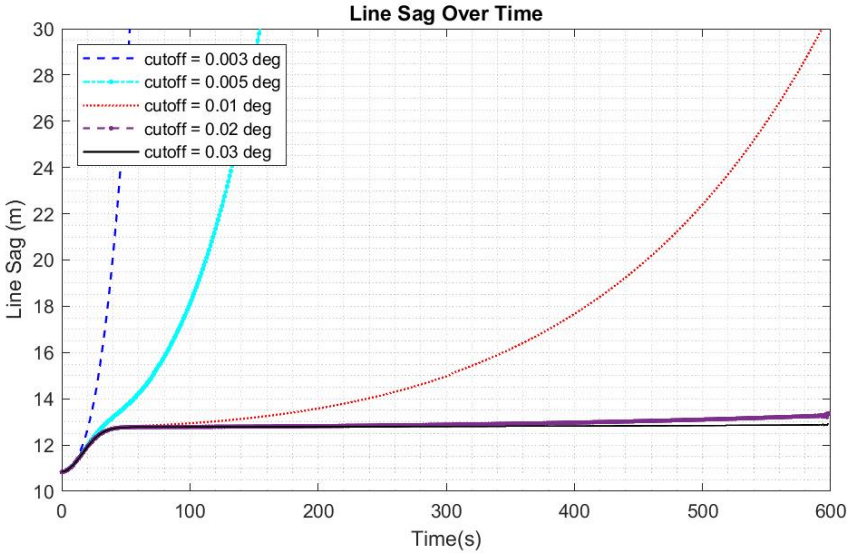

Figure 4.16: Line Sag Overtime with Seven Different Cutoff Distances.

Figure 4.16 shows the line sag curves over time with seven different cutoff distances from the center of the fire to the center of the closest power line segments to the fire. It is generated using MATLAB with the highest wind speed and fire rate of spread resulted from BehavePlus. The wind speed stays at 5.6 m/s and the fire rate of spread is held at 0.29 m/s. The cutoff distances vary from 0.003 decimal degrees longitude and latitude to 0.03 decimal degrees longitude and latitude. When the fire spreads and reaches the power line segment during the simulation, the convective heat gain from the fire to the line is also considered in the heat transfer model. The graphs

indicate that line sag increases as the distance cutoff range reduces. Note that 0.01 degrees longitude equates to 1.11 km and 0.01 degrees latitude equates to about 0.91 km.

Chapter 5

CONCLUSION

In this paper, a technique that leverages the existing power system infrastructure to detect wildfires during an early stage is proposed. It involves the use of line sag sensors like Ampacimon's sense to make measurements on the power line sag in real-time based on the conductor vibration and the span's fundamental frequencies.

Through the course of this research, the heat transfer model and algorithm are able to show a significant difference between the line sag under normal condition and the line sag under a fire event. The line sag increases almost exponentially under a wildfire event for a period of 600 seconds. The results show that line sensors should be able to detect a potential fire hazard based on the irregular sag behavior within 150 seconds.

A limitation is that the sensors are rated only up to 200 $^{\circ}C$, which means it may be damaged or make inaccurate measurements once the conductor temperature and/or the ambient temperature reaches 200 $^{\circ}C$. This paper also takes into account of the limitation and suggests the use of fire-resistant materials like silica fibers to be attached to the sensor surface. A FEMM model of the three-phase electrical power lines is then created. It simulates the magnetic fields of the lines before and after the application of silica fabrics to determine whether they will affect the magnetic fields of the conductors. Given the negligible difference, it is decided that silica fibers are great shields for thermal protection of the line sensors.

The paper then looks closely at how the 20-ft wind speed and wind direction changes affect the crown fire rate of spread in the simulation and how they impact

in different power line sag over 600 seconds. The effects of the different fire-starting location on the aerial map on the line sag is also studied in section 5. It is concluded that while the increase in wind angle from 0 to 90 degrees causes an increase in line sag, the line sag does not have a direct, simple, or linear relationship with the change in wind speed. It is rather more complicated due to the fact that the increase of wind speed increases the fire rate of spread but at the same time reduces the convective heat loss. Lastly, when then fire-starting location gets closer to the line segment and the fire does spread and reach the line, the line sag increases significantly and much quicker.

From the simulation results, it is concluded that there are a few ways in detecting a starting fire or a potential fire hazard. One of them is detecting a hazard when the line sag reaches the 25-meter threshold or the minimum clearances from ground. Another method is through real-time monitoring, a threshold is set for the difference between the line sag measurements in real-time and the calculated line sag during normal conditions. When this threshold is reached, a potential fire hazard can be detected. The shorter detection time should be the determining factor in which method to use for early wildfire detection.

Overall, the research results indicate that line sag sensors are good alternatives to other early forest fire detection technologies because most utilities already have line sag sensors installed on the transmission lines. They should be incorporated also based on their affordability, reliability, and simplicity.

Chapter 6

FUTURE RECOMMENDATIONS

In the future, the dynamics of wind and its effects on the expansion of the fire should be studied more in depth. Using this model, it is possible to use the direction of the wind to predict fire movement and expansion. Thus, theoretically the fire's movement can be tracked through analyzing the sag change of nearby power lines, with appropriate assumptions to model the fire behavior and parameters.

Lab experiments should be done to verify the assumptions made and the results. This is still difficult to do on a laboratory-scale, hence it is better to perform the experiments with utilities involved because they have a lot more resources and information available to access real-time measurements.

Additionally, wildfire behavior is so unpredictable depending on various factors like wind speed and fuel sources. Therefore, a more realistic fire model should be created to be integrated to the grid and heat transfer model. Applying the topology of the map also helps better predict fire behavior because irregular slopes affect the direction and rate of fire spread.

Most of the researched fire detection technologies are rather passive, meaning actions are taken after a fire is sparked. In addition, preventative actions should be considered to eliminate the cause of a potential fire hazard. One instance is forest management, which includes prescribed burning. Prescribed burning helps remove fine fuels like needles, shrubs, and excess debris. Local and state building design standards and guidelines should also be improved to use more fire-resistant materials in buildings.

Most importantly, it requires us to take individual actions to combat climate change, which is a main cause of higher temperature and drying vegetation. Wildfires are more frequent and intense due to climate change. We should try to reduce carbon emissions in our everyday lives using electric vehicles, solar panels, and other renewable energy sources. Moreover, we should extinguish fire pits and campfires completely and clean up the used area when done. Paying attention to any risk of fires in local areas helps prevent any fire-prone activities and protect ourselves.

BIBLIOGRAPHY

[1] " Energy Commission, Cartography Unit, U.S. Census Bureau, Cal-Atlas," california energy commission. [Online]. Available at https://cecgis-caenergy.opendata.arcgis.com/datasets/260b4513acdb4a3a8e4d64e69fc84fee_0/data?geometry=-133.637%2C34.336%2C-103.622%2C40.44. [Accessed: 2019-07-30].

[2] "Aluminum 6061-T6; 6061-T651," asm aerospace specification metals inc.,. [Online]. Available at http://asm.matweb.com/search/SpecificMaterial.asp?bassnum=MA6061T6. [Accessed: 2020-12-20].

[3] "Aluminum 6061-T6; 6061-T651," www.matweb.com,. [Online]. Available at http://www.matweb.com/search/datasheet_print.aspx?matguid=1b8c06d0ca7c456694c7777d9e10be5b. [Accessed: 2020-12-20].

[4] "Ampacimon Data Sheet, Real Time Thermal Rating, Dynamic Line Rating". [Accessed: 2019-07-30].

[5] "behaveplus tech tips,". [Accessed: 2021-02-01].

[6] "California's Forest Resources: Forest Inventory and Analysis,". [Online]. Available at https://www.fs.fed.us/pnw/pubs/pnw_gtr913.pdf. [Accessed: 2019-08-27].

[7] "chapter 5: Installation practices,". [Accessed: 2021-02-01].

[8] "handbook: Fuel moisture,". [Online]. Available at http://factsheets.okstate.edu/e1010/sections/fuel-moisture/. [Accessed: 2021-02-01].

[9] "MatWeb: Online Material Information Resource," www.matweb.com,. [Accessed: 2020-12-20].

[10] "NIST Fire Research Division, Fire Dynamics,". [Online]. Available at `https://www.nist.gov/el/fire-research-division-73300`. [Accessed: 2019-07-30].

[11] "UIUC 150-Bus System," illinois information trust institute,. [Online]. Available at `https://icseg.iti.illinois.edu/synthetic-power-cases/uiuc-150-bus-system/`. [Accessed: 2019-05-20].

[12] Firms faq, 2019.

[13] A. Alkhatib. "a review on forest fire detection techniques,". pages 1–12, 3 2014. [Accessed: 2019-09-20].

[14] S. Aslan, U. Güdükbay, B. U. Töreyin, and A. Enis Çetin. "Early Wildfire Smoke Detection Based on Motion-based Geometric Image Transformation and Deep Convolutional Generative Adversarial Networks,". In *ICASSP 2019 - 2019 IEEE International Conference on Acoustics, Speech and Signal Processing (ICASSP)*, pages 8315–8319, May 2019.

[15] B. Chen, K. L. Butler-Purry, and D. Kundur. "Impact analysis of transient stability due to cyber attack on FACTS devices,". In *2013 North American Power Symposium (NAPS)*, pages 1–6, Sept 2013.

[16] E. Cloet and J. Lilien. "Uprating Transmission Lines through the use of an innovative real-time monitoring system,". In *2011 IEEE PES 12th International Conference on Transmission and Distribution Construction, Operation and Live-Line Maintenance (ESMO)*, pages 1–6, May 2011.

[17] E. Cloet and J.-l. Lilien. "Uprating Transmission Lines Through the Use of an Innovative Real-Time Monitoring System,". pages 1–6, 05 2011.

[18] K. R. Davis, K. L. Morrow, R. Bobba, and E. Heine. "Power Flow Cyber Attacks and Perturbation-based Defense,". In *2012 IEEE Third International Conference on Smart Grid Communications (SmartGridComm)*, pages 342–347, Nov 2012.

[19] D. Deka, R. Baldick, and S. Vishwanath. "Optimal Data Attacks on Power Grids: Leveraging Detection Measurement Jamming,". *CoRR*, abs/1506.04541, 2015.

[20] R. Deng, G. Xiao, and R. Lu. "Defending Against False Data Injection Attacks on Power System State Estimation,". *IEEE Transactions on Industrial Informatics*, 13(1):198–207, Feb 2017.

[21] M. T. Devine and P. Cuffe. "Blockchain Electricity Trading Under Demurrage,". *IEEE Transactions on Smart Grid*, 10(2):2323–2325, March 2019.

[22] E. Erickson, R. Slobodin, M. Poshtan, T. Taufik, and J. Callenes. "using power infrastructures for wildfire detection in california,". pages 1–5, 9 2019.

[23] R. Ellis. "why the california wildfires are spreading so quickly," cnn.com. [Online]. Available at `https://www.cnn.com/2018/11/09/us/wildfires-why-they-spread-so-quickly-wcx/index.html`, 11 2018. [Accessed: 2019-09-20].

[24] D. D. et al. "IEEE Standard for Calculating the Current-Temperature Relationship of Bare Overhead Conductors,". page 6, 10 2012.

[25] C. S. et all. "PGE slammed for cutting power to millions of Californians," cnbcnews.com,. [Online]. Available at https://www.nbcnews.com/news/us-news/pg-e-slammed-cutting-power-millions-californians-n1064481/, 10 2019. [Accessed: 2019-12-20].

[26] E. C. et all. "Experiences of the Belgian and French TSOs using the "Ampacimon" real-time dynamic rating system,". page 4, 2010.

[27] H. F. et all. "city and state declare emergencies as saddlerideg fire burns homes in the valley,". pages 1–3, 10 2019. [Accessed: 2019-06-20].

[28] J. S. et all. "Detection of smoke plume for a land-based early forest fire detection system,". page 959907, 09 2015.

[29] J. X. et all. "Early forest-fire detection using scanning polarization lidar,". *Applied Optics*, 09(28), 9 2020.

[30] M. H. et all. "Complex Permittivity and Permeability of SiQ2 and FeO4 Powders in Microwave Frequency Range Between 0.2 and 13.5 GHz,". volume 49, pages 1443–1448, May 2009.

[31] Y. C. et all. "A UAV-based Forest Fire Detection Algorithm Using Convolutional Neural Network,". In *2018 37th Chinese Control Conference (CCC)*, pages 10305–10310, July 2018.

[32] B. . Gao, X. Xiong, and R. . Li. "A Study of MODIS Fire Detecting Channel Centered at 3.95-m,". In *2006 IEEE International Symposium on Geoscience and Remote Sensing*, pages 1100–1102, July 2006.

[33] J. Golubovskaya. "Resistivity of Glass," hypertextbook.com. [Online]. Available at

https://hypertextbook.com/facts/2004/JaneGolubovskaya.shtml, 2004. [Accessed: 2020-01-15].

[34] L. L. Grigsby. *eonard*. CRC Press, 2012.

[35] hcbiochem. "compare and explain the electrical conductivities of sodium and sodium oxide in the solid and liquit states," uk.answers.yahoo.com. [Online]. Available at https://uk.answers.yahoo.com/question/index?qid=20111206064001AAXPDNI, 2011. [Accessed: 2020-01-15].

[36] A. M. Helmenstine. "How to Melt Aluminum Cans at Home," thoughtco.com. [Online]. Available at https://www.thoughtco.com/melt-aluminum-cans-at-home-608277, 08 2019. [Accessed: 2019-12-20].

[37] Z. Huang, S. Etigowni, L. Garcia, S. Mitra, and S. Zonouz. "Algorithmic Attack Synthesis Using Hybrid Dynamics of Power Grid Critical Infrastructures,". In *2018 48th Annual IEEE/IFIP International Conference on Dependable Systems and Networks (DSN)*, pages 151–162, June 2018.

[38] e. a. J. Fan. "Mitigating Stealthy False Data Injection Attacks Against State Estimation in Smart Grid,". In *2018 IEEE Conference on Communications and Network Security (CNS)*, pages 1–9, May 2018.

[39] J. D. J. L Lilien. "device, system and method for real-time monitoring of overhead power lines,", 5 U.S. Patent 8184015 B2. [Accessed: 2021-02-01].

[40] M. Jin, J. Lavaei, and K. H. Johansson. "Power Grid AC-based State Estimation: Vulnerability Analysis Against Cyber Attacks,". *IEEE Transactions on Automatic Control*, pages 1–1, 2018.

[41] S. W. Kieffer. "Megafires: the New Moon," geologiinmotion.com,. [Online]. Available at http://www.geologyinmotion.com/2013/10/megafires-new-norm.html/, 10 2019. [Accessed: 2019-12-20].

[42] Kishugu. "Command and Control - the modern day role of the Spotter Plane," kishugu.com,. [Online]. Available at https://kishugu.com/command-and-control-the-modern-day-role-of-the-spotter-plane/?cn-reloaded=1/, 07 2018. [Accessed: 2019-12-20].

[43] N. Kshetri and J. Voas. "Hacking Power Grids: A Current Problem,". *Computer*, 50(12):91–95, December 2017.

[44] S. Lakshminarayana and D. K. Y. Yau. "Cost-Benefit Analysis of Moving-Target Defense in Power Grids,". *CoRR*, abs/1804.01472, 4 2018.

[45] Li Guang-Hui, Zhao Jun, and Wang Zhi. "Research on Forest Fire Detection Based on Wireless Sensor Network,". In *2006 6th World Congress on Intelligent Control and Automation*, volume 1, pages 275–279, June 2006.

[46] E. Lindberg. "The Overhead Line Sag Dependence on Weather Parameters and Line Current,". *Examensarbete 30 hp UPTEC vol. W11 no. 017*, December 2011.

[47] S. Liu, X. P. Liu, and A. E. Saddik. "Denial-of-Service (dos) attacks on load frequency control in smart grids,". In *2013 IEEE PES Innovative Smart Grid Technologies Conference (ISGT)*, pages 1–6, Feb 2013.

[48] Y. Liu, M. K. Reiter, and P. Ning. "False data injection attacks against state estimation in electric power grids,". *ACM Trans. Inf. Syst. Secur.*, 14:13:1–13:33, 2009.

[49] K. Pan, A. Teixeira, C. D. López, and P. Palensky. "Co-simulation for cyber security analysis: Data attacks against energy management system,". In *2017 IEEE International Conference on Smart Grid Communications (SmartGridComm)*, pages 253–258, Oct 2017.

[50] B. Quayle. "Fire Detective Maps," USDA Forest Service,". [Online]. Available at `https://fsapps.nwcg.gov/`, 01 2017. [Accessed: 2019-01-20].

[51] A. Reyes-Velarde. "California's Camp fire was the costliest global disaster last year, insurance report shows," los angeles times. [Online]. Available at `https://www.latimes.com/local/lanow/la-me-ln-camp-fire-insured-losses-20190111-story.html`, 01 2019. [Accessed: 2019-01-20].

[52] R. C. Rothermel. "A mathematical model for predicting fire pread in wildland fuels,". In *Res. Pap. INT-115. Ogden, UT: U.S. Department of Agriculture, Forest Service, Intermountain Forest and Range Experiment Station*, page 40, 1972.

[53] R. C. Rothermel. "Predicting behavior and size of crown fires in the northern Rocky Mountains,". In *Res. Pap. RMRS-RP-29. Fort Collins, CO: U.S. Department of Agriculture, Forest Service, Rocky Mountain Research Station*, page 46, 1991.

[54] e. a. Saqib Hasan. "Vulnerability Analysis of Power Systems Based on Cyber-Attack and Defense Models,". In *ISGT*, Washington DC, 02/2018 2018. IEEE, IEEE.

[55] D. Schroeder. "Evaluation of Three Wildfire Smoke Detection Systems,". volume 5, pages 1–8, June 2004.

[56] D. Shelar, P. Sun, S. Amin, and S. Zonouz. "Compromising Security of Economic Dispatch in Power System Operations,". In *2017 47th Annual*

IEEE/IFIP International Conference on Dependable Systems and Networks (DSN), pages 531–542, June 2017.

[57] J. Slegers. "Transmission Line Loading: Sag Calculations and High-Temperature Conductor Technologies,", 2011.

[58] Southwire. *"Southwire ACSR Series Wire: Aluminum Conductor. Steel Reinforced. Bare,"*, 2003. [Accessed: 2019-05-20].

[59] S. Sridhar, A. Hahn, and M. Govindarasu. "Cyber–Physical System Security for the Electric Power Grid,". *Proceedings of the IEEE*, 100(1):210–224, Jan 2012.

[60] L. Thomas. "what is silica fiber," wisegeek.com. [Online]. Available at `https://www.wisegeek.com/what-is-silica-fiber.htm`, 12 2020. [Accessed: 2020-12-20].

[61] O. Vukovic and G. Dan. "Security of Fully Distributed Power System State Estimation : Detection and Mitigation of Data Integrity Attacks,". *IEEE Journal on Selected Areas in Communications*, 32(7):1500–1508, 2014. QC 20140924.

[62] C. Wressnegger, A. Kellner, and K. Rieck. "ZOE: Content-Based Anomaly Detection for Industrial Control Systems,". In *2018 48th Annual IEEE/IFIP International Conference on Dependable Systems and Networks (DSN)*, pages 127–138, June 2018.

[63] M. Wydra and P. Kacejko. "Power system state estimation using wire temperature measurements for model accuracy enhancement,". In *2016 IEEE PES Innovative Smart Grid Technologies Conference Europe (ISGT-Europe)*, pages 1–6, Oct 2016.

[64] e. a. Y. Huang. "State Estimation in Electric Power Grids: Meeting New Challenges Presented by the Requirements of the Future Grid,". *IEEE Signal Processing Magazine*, 29(5):33–43, Sept 2012.

[65] R. D. Zimmerman, C. E. Murillo-Sanchez, and R. J. Thomas. "MATPOWER: Steady-State Operations, Planning, and Analysis Tools for Power Systems Research and Education,". *IEEE Transactions on Power Systems*, 26(1):12–19, Feb 2011.

APPENDICES

Appendix A

MATLAB SCRIPTS

Main.m

```
1  % This code access the Tennessee 150-bus synthetic grid, performs power
2  % flow analysis using MATPOWER, and outputs electrical currents. It maps
3  % the grid based on geographical information provided and calculated the
4  % distances between a randomly generated fire location and the center of
5  % each line span segment. Only three of the closest line segments are
6  % considered and plotted to analyze the line temperature and line sag
7  % changes over simulation time.
8  % Run the Main.m code 4 times to get the exact fire location as the report.
9  % Author: Virginia Yan date: 2021/01/19
10 clear; clc; close all;
11 global simTime earthRadiusInMeters OD condRadius Towerheight Ta fSpeed N Ns
       F...
12 V_w phi fTemp TcThreshold cs ca ma ms mc emissivity stefan_boltz
      absorptivity...
13 k_sk alpha Rdc He
14
15 setGlobal % setting parameters
16
17 % import coordinates of the substations
18 coordinates = readmatrix('uiuc-150bus.csv');
19 subToBus = readmatrix('uiuc-150bus-subToBus.csv');
```

```
20
21 for i = 1:150
22 busCoords(i,:) = [coordinates(subToBus(i,3), 4) coordinates(subToBus(i,3),
       3)];
23 end
24
25 ieee = {'uiuc_150bus'}; grids = [ieee];
26
27 for i=1:length(grids)
28 mpc = loadcase(char(grids(i))); %load testcase data
29 NumberedSystem = ext2int(runpf(mpc)); %run power flow and save results
30 figure(1)
31 g = graph(mpc.branch(:,1), mpc.branch(:,2));
32 gplot(adjacency(g), busCoords);
33 xlabel('Longitude (deg)')
34 ylabel('Latitude (deg)')
35 axis equal
36 hold on
37
38 for i=1 : length(busCoords) %by bus indexing
39 delP(i) = NumberedSystem.branch(i,14)-NumberedSystem.branch(i,16);
40 delQ(i) = NumberedSystem.branch(i,15)-NumberedSystem.branch(i,17);
41 if (delP(i) == delQ(i))&& (delQ(i)== 0)
42 bus(i).current = 0;
43 continue;
44 end
45 end
46
```

```
47 for i=1 : length(mpc.branch(:,1)) %by line indexing
48 % rearrange the TL terminal coordinates from left to right
49 % busCoords(mpc.branch(j,1),1) is longitude
50 if (busCoords(mpc.branch(i,1),1) < busCoords(mpc.branch(i,2),1)) % compare
       longitudes
51 if (busCoords(mpc.branch(i,2),1) > busCoords(mpc.branch(i,2),2)) % compare
       lat
52 buses.lines(i).coords(1:2) = busCoords(mpc.branch(i,2),:);
53 buses.lines(i).coords(3:4) = busCoords(mpc.branch(i,1),:);
54 else
55 buses.lines(i).coords(1:2) = busCoords(mpc.branch(i,1),:);
56 buses.lines(i).coords(3:4) = busCoords(mpc.branch(i,2),:);
57 end
58 elseif (busCoords(mpc.branch(i,1),1) >= busCoords(mpc.branch(i,2),1))
59 if (busCoords(mpc.branch(i,2),1) < busCoords(mpc.branch(i,2),2))
60 buses.lines(i).coords = [busCoords(mpc.branch(i,2),:), busCoords(mpc.branch
       (i,1),:)];
61 else
62 buses.lines(i).coords(1:2) = busCoords(mpc.branch(i,1),:);
63 buses.lines(i).coords(3:4) = busCoords(mpc.branch(i,2),:);
64 end
65 end
66
67 if (buses.lines(i).coords(1) == buses.lines(i).coords(3))&&(buses.lines(i).
       coords(2) == buses.lines(i).coords(4)) % compare lat
68 buses.lines(i).coords(:) = [0,0,0,0];
69 end
70
```

```
71 [buses.lines(i).length, buses.lines(i).azimuth] = distance(buses.lines(i).
       coords(2),buses.lines(i).coords(1),buses.lines(i).coords(4),buses.lines
       (i).coords(3),earthRadiusInMeters);
72 end
73
74 %% preallocation
75 span = zeros(1,178); NumTLseg = zeros(1,178); lineAngle = zeros(1,178);
76 condTerminalX = zeros(178,426); condTerminalY = zeros(178,426); condCenterX
        = zeros(178,425);
77 condCenterY = zeros(178,425);
78
79 % divide the transmission line
80 Idealspan = 250;
81 for i = 1:178
82 if buses.lines(i).length == 0
83 span(i) = 0;
84 NumTLseg(i) = 0;
85 else
86 % first divide TL by min length between towers
87 NumTLseg(i) = floor(buses.lines(i).length/Idealspan);
88 remainderLen = rem(buses.lines(i).length,Idealspan);
89 span(i) = Idealspan + remainderLen/NumTLseg(i);
90 end
91
92 % obtain conductor coordinates to calculate the center
93 if buses.lines(i).length == 0
94 lineAngle(i) = 0;
95 elseif buses.lines(i).coords(2) > buses.lines(i).coords(4)
```

```
 96 lineAngle(i) = 180 - atand((buses.lines(i).coords(2)-buses.lines(i).coords
        (4))/(abs(buses.lines(i).coords(1)-buses.lines(i).coords(3)))); % get
        the line angle from aerial map
 97 elseif buses.lines(i).coords(2) < buses.lines(i).coords(4)
 98 lineAngle(i) = atand((buses.lines(i).coords(4)-buses.lines(i).coords(2))/(
        buses.lines(i).coords(3)-buses.lines(i).coords(1)));
 99 elseif buses.lines(i).coords(2) == buses.lines(i).coords(4)
100 lineAngle(i) = 0;
101 end
102 end
103
104 for i = 1:178
105 if buses.lines(i).length == 0
106 del_x = 0; del_y = 0;
107 elseif buses.lines(i).coords(2) > buses.lines(i).coords(4)
108 del_x = span(i)*cosd(180-lineAngle(i));
109 del_y = span(i)*sind(180-lineAngle(i));
110 else
111 del_x = span(i)*cosd(lineAngle(i));
112 del_y = span(i)*sind(lineAngle(i));
113 end
114
115 % need to convert del_x and del_y from meter to deg first
116 del_x = rad2deg(del_x/earthRadiusInMeters); % in degrees
117 del_y = rad2deg(del_y/earthRadiusInMeters);
118
119 for k = 1:NumTLseg(i)+1
120 if k == 1
```

```
121 condTerminalX(i,k) = buses.lines(i).coords(1); % in deg not in m
122 condTerminalY(i,k) = buses.lines(i).coords(2); % in deg not in m
123 else
124 % since longitude is negative, need to subtract del_x
125 condTerminalX(i,k) = condTerminalX(i,k-1) + del_x;
126
127 if buses.lines(i).coords(2) > buses.lines(i).coords(4)
128 condTerminalY(i,k) = condTerminalY(i,k-1) - del_y;
129 else
130 condTerminalY(i,k) = condTerminalY(i,k-1) + del_y;
131 end
132 end
133 end
134 % calculate the center point of each conductor segment
135 if buses.lines(i).length == 0
136 condCenterX(i,k) = 0;
137 condCenterY(i,k) = 0;
138 else
139 for k = 1:NumTLseg(i)
140 condCenterX(i,k) = (condTerminalX(i,k)+ condTerminalX(i,k+1))/2;% lon in
        deg
141 condCenterY(i,k) = (condTerminalY(i,k)+ condTerminalY(i,k+1))/2;% lat in
        deg
142 end
143 end
144 end
145
146 %% generate a random fire location on the network
```

```
147 flag = 1;
148 while flag <= 5 % 5 repetitions
149 x = randi([1 178],1,1); y = randi([1 476],1,1);
150 if condCenterX(x,y) ~= 0
151 rng default
152 % 0.02deg lon equates to 2.22km and 0.02deg lat equate to 1.82km
153 % https://stackoverflow.com/questions/639695/how-to-convert-latitude-or-
        longitude-to-meters
154 fire(1) = abs( condCenterX(x,y)+0.01 - (condCenterX(x,y)-0.01)).* rand(1,1)
         + condCenterX(x,y)-0.01; %generate random x coordinate; lon
155 rng default
156 fire(2) = abs( condCenterY(x,y)+0.01 - (condCenterY(x,y)-0.01)).* rand(1,1)
         + condCenterY(x,y)-0.01; %generate random y coordinate
157 break
158 else
159 flag = flag + 1;
160 end
161 end
162 plot(fire(1), fire(2),'r^');
163 % annotation('rectangle',[0.5 0.51 0.03 0.03]);
164 saveas(gcf,[pwd '/Results/','AerialMap.fig'])
165 saveas(gcf,[pwd '/Results/','AerialMap.jpg'])
166 delete(findall(gcf,'type','annotation'))
167
168 [P,Q]=size(condCenterX); % P = 178
169 for i=1 : P
170 if (buses.lines(i).length == 0)
171 buses.lines(i).center = 0; buses.lines(i).current = 0;
```

```
172 else
173
174 buses.lines(i).center = midPoint(buses.lines(i).coords(1:2), buses.lines(i)
        .coords(3:4)); %calculate the center point of each line
175 text((buses.lines(i).center(1)), (buses.lines(i).center(2)), int2str(i), '
        Clipping', 'on');
176 xlim([fire(1)-0.5 fire(1)+0.5])
177 ylim([fire(2)-0.5 fire(2)+0.5])
178 saveas(gcf,[pwd '/Results/','AerialMapwithLabels.fig'])
179 saveas(gcf,[pwd '/Results/','AerialMapwithLabels.jpg'])
180 % calculate the line currents from the power flow results
181 MWFromBus = abs(NumberedSystem.branch(i,14));
182 MVARFromBus = abs(NumberedSystem.branch(i,15));
183 pf = MWFromBus/sqrt((MWFromBus^2) + (MVARFromBus^2));
184 %find corresponding bus voltages
185 fromBusVoltage = NumberedSystem.bus(NumberedSystem.branch(i,1), 8) *
        NumberedSystem.bus(NumberedSystem.branch(i,1), 10);
186 buses.lines(i).current = MWFromBus/(sqrt(3) * pf * fromBusVoltage)* 1000;
187 end
188 end
189
190 centerDist = zeros(178,425); fireToCenter = zeros(178,425); finalTheta =
        zeros(178,425); wires = zeros(178,425);
191 sag = zeros(178,425); sagSteps = zeros(178,425); theta = zeros(178,425);
192 aff = 0; w = 1;
193
194 for i = 1:P
195 % calculate the distance between fire and conductor segment
```

```
196 % centers: centerDist
197 for k = 1:NumTLseg(i)
198 if buses.lines(i).length == 0
199 centerDist(i,k) = 0;fireToCenter(i,k) = 0; finalTheta(i,k) = 0; wires{i}=0;
        sag{i}=0; sagSteps(i)=0;
200 else
201 % https://www.mathworks.com/help/map/calculate-distance-between-two-points-
        in-geographic-space.html
202 % https://www.mathworks.com/help/map/working-with-distances-on-the-sphere.
        html
203 centerDist(i,k) = distance(fire(2), fire(1), condCenterY(i,k), condCenterX(
        i,k), earthRadiusInMeters); % in meters
204
205 % heat transfer function
206 aff = aff+1; % w should be the number of lines affected
207 % theta is the angle bt fire and center of conductor segment
208 if buses.lines(i).coords(2) < buses.lines(i).coords(4)
209 if (fire(2) > condCenterY(i,k)) & (fire(1) > condCenterX(i,k))
210 phi = atand (abs(fire(2)-condCenterY(i,k)) / (abs(fire(1)-condCenterX(i,k))
        ));
211 theta(i,k) = abs(phi - lineAngle(i));
212 elseif (fire(2) > condCenterY(i,k)) & (fire(1) < condCenterX(i,k))
213 phi = atand (abs(fire(2)-condCenterY(i,k)) / (abs(fire(1)-condCenterX(i,k))
        ));
214 theta(i,k) = abs(phi - lineAngle(i));
215 elseif (fire(2) < condCenterY(i,k)) & (fire(1) < condCenterX(i,k))
216 phi = atand (abs(fire(2)-condCenterY(i,k)) / (abs(fire(1)-condCenterX(i,k))
        ));
```

```
217 theta(i,k) = abs(lineAngle(i) - phi);
218 elseif (fire(2) < condCenterY(i,k)) & (fire(1) > condCenterX(i,k))
219 phi = atand (abs(fire(2)-condCenterY(i,k)) / (abs(fire(1)-condCenterX(i,k))
       ));
220 theta(i,k) = abs(phi + lineAngle(i));
221 elseif (fire(1) == condCenterX(i,k)) % if x coordinates of fire and center
       are equal
222 phi = 0; % should be infinite but just make it zero for now since it's
       irrelevant to theta
223 theta(i,k) = abs(90 - lineAngle(i));
224 end
225 else
226 if (fire(2) > condCenterY(i,k)) & (fire(1) > condCenterX(i,k))
227 phi = atand (abs(fire(2)-condCenterY(i,k)) / (abs(fire(1)-condCenterX(i,k))
       ));
228 theta(i,k) = abs(phi - lineAngle(i));
229 elseif (fire(2) < condCenterY(i,k)) & (fire(1) < condCenterX(i,k))
230 phi = atand (abs(fire(2)-condCenterY(i,k)) / (abs(fire(1)-condCenterX(i,k))
       ));
231 theta(i,k) = abs(lineAngle(i) - phi);
232 elseif (fire(2) > condCenterY(i,k)) & (fire(1) < condCenterX(i,k))
233 phi = atand (abs(fire(2)-condCenterY(i,k)) / (abs(fire(1)-condCenterX(i,k))
       ));
234 theta(i,k) = phi + lineAngle(i);
235 if theta(i,k) > 180
236 theta(i,k) = theta(i,k) - 180;
237 end
238 elseif (fire(2) < condCenterY(i,k)) & (fire(1) > condCenterX(i,k))
```

```
239 phi = atand (abs(fire(2)-condCenterY(i,k)) / (abs(fire(1)-condCenterX(i,k))
        ));
240 theta(i,k) = phi + lineAngle(i);
241 if theta(i,k) > 180
242 theta(i,k) = theta(i,k) - 180;
243 end
244 elseif (fire(1) == condCenterX(i,k)) % if x coordinates of fire and center
        are equal
245 phi = 0; % should be infinite but just make it zero for now since it's
        irrelevant to theta
246 theta(i,k) = abs(lineAngle(i) - 90);
247 end
248 end
249 end
250 end
251 end
252
253 % find the closest conductor segments and the index
254 for i = 1:P
255 c = centerDist(i,:);
256 c(centerDist(i,:)==0) = NaN;
257 m(i) = min(c(:)); % min centerDist
258 % go to the closest TL to find the closest conductor segment
259 Ind{i} = find(centerDist(i,:) == m(i));% returns the closest conductor
        segment
260 end
261
262 % MinDist shows the shortest path bt center of fire and TL segments
```

```
263 [MinDist,closestTL] = mink(m,3);% lineLen is 3 closest TL's (closestTL)
        with the line lengths
264 end
265
266 fRadius = 0.5 + fSpeed*(0:simTime-1);
267 %% calculates view factor and select latitude for solar radiation
268 % Num = 110;
269 for c = 1:length(fRadius)
270 % figure(Num);
271 [fArea(c), fCoords] = FireCalc(fRadius(c)); % fire area expands and fire
        coords change
272 for a = 1:3
273 % get the closest line segment to the fire from the furthest TL;
274 ind = closestTL(a); % returns jus 14, 171, 172
275 in = Ind{closestTL(a)}; % returns just 84, 73, 21
276 dist(a,c) = MinDist(a)-fSpeed*(c-1);
277 ClosestSpan(a) = span(ind);
278 [x,y,z] = pol2cart(180-theta(ind,in), dist(a,c), Towerheight);% coordinates
         of center of the line segment
279 x2 = x + ClosestSpan(a)*cosd(theta(ind,in)-90)/2;
280 y2 = y + ClosestSpan(a)*sind(theta(ind,in)-90)/2;
281 x1 = x - ClosestSpan(a)*cosd(theta(ind,in)-90)/2;
282 y1 = y - ClosestSpan(a)*sind(theta(ind,in)-90)/2;
283 topLeft = [x1,y1+condRadius, Towerheight]; %calculate coordinates for the
        top left of segment
284 topRight = [x1, y1-condRadius, Towerheight]; %calculate coordinates for the
         top right of segment
```

```
285 bottomLeft = [x2, y2+condRadius, Towerheight]; %calculate coordinates for
        the bottom left of segment
286 bottomRight = [x2, y2-condRadius, Towerheight]; %calculate coordinates for
        the bottom right of segment
287 SegCoords = [topLeft; topRight; bottomRight; bottomLeft]; %return the
        coordinates calculated
288 % plot3(SegCoords(:,1),SegCoords(:,2),SegCoords(:,3)); hold on
289 VF(a,c) = ViewFactor(fCoords, SegCoords,2); % calculates view factor
290 latitude(a) = min([condTerminalY(ind,in) condTerminalY(ind,in+1)]) + (max([
        condTerminalY(ind,in) condTerminalY(ind,in+1)])- min([condTerminalY(ind
        ,in) condTerminalY(ind,in+1)])).*rand(1,1); % latitude randomly
        selected between the closest segment
291 RelativeDist(a,c) = dist(a,c)/fRadius(c);
292 end
293 % plot3(fCoords(:,1),fCoords(:,2),fCoords(:,3)); hold off% plots
294 % the fire expanding
295 end
296
297 %% no fire heat transfer simulation
298 % PLOTS VIEW FACTOR VS RELATIVE DISTANCE WITH FIRE EXPANDING
299 fRadius_N = 0.5+ 0*(0:simTime-1);
300 for c = 1:length(fRadius_N)
301 [fArea_N(c), fCoords_N] = FireCalc(fRadius_N(c)); % fire area expands and
        fire coords change
302 for a = 1:3
303 % get the closest line segment to the fire from the furthest TL;
304 ind = closestTL(a);
305 in = Ind{closestTL(a)};
```

```
306 dist_N(a,c) = MinDist(a)-fSpeed*(c-1);
307 ClosestSpan(a) = span(ind);
308 [x_N,y_N,z_N] = pol2cart(180-theta(ind,in), dist_N(a,c), Towerheight);%
        coordinates of center of the line segment
309 x2_N = x_N + ClosestSpan(a)*cosd(theta(ind,in)-90)/2;
310 y2_N = y_N + ClosestSpan(a)*sind(theta(ind,in)-90)/2;
311 x1_N = x_N - ClosestSpan(a)*cosd(theta(ind,in)-90)/2;
312 y1_N = y_N - ClosestSpan(a)*sind(theta(ind,in)-90)/2;
313 topLeft_N = [x1_N,y1_N+condRadius, Towerheight]; %calculate coordinates for
         the top left of segment
314 topRight_N = [x1_N, y1_N-condRadius, Towerheight]; %calculate coordinates
        for the top right of segment
315 bottomLeft_N = [x2_N, y2_N+condRadius, Towerheight]; %calculate coordinates
         for the bottom left of segment
316 bottomRight_N = [x2_N, y2_N-condRadius, Towerheight]; %calculate
        coordinates for the bottom right of segment
317 SegCoords_N = [topLeft_N; topRight_N; bottomRight_N; bottomLeft_N]; %return
         the coordinates calculated
318 VF_N(a,c) = ViewFactor(fCoords_N, SegCoords_N,2); % calculates view factor
319 RelativeDist_N(a,c) = dist_N(a,c)/fRadius_N(c);
320 end
321 end
322
323 Tc_N = zeros(1,600); del_T_N = zeros(1,600);
324 del_sag_N = zeros(1,600); sag_N = zeros(1,600);
325
326 for b = 1:3
327 ClosestSegNum(b) = Ind{closestTL(b)};
```

```
328 ind = closestTL(b);
329 [del_T_N(b,:), Tc_N(b,:), sag_N(b,:), del_sag_N(b,:)] = heatTransferNormal(
        latitude(b), buses.lines(ind).azimuth, buses.lines(ind).current,
        ClosestSpan(b));
330 end
331
332 % take out zeros
333 Tc_N(Tc_N==0)=nan; del_T_N(del_T_N==0)=nan; del_sag_N(del_sag_N==0)=nan;
        sag_N(sag_N==0)=nan;
334
335 % calculates time constant
336 for i = 1:3
337 TC(i) = Tc_N(i,600)*.632;
338 end
339
340 % HEAT TRANSFER WITH FIRE
341 Qj = zeros(1,600); Qs = zeros(1,600); Qr = zeros(1,600);
342 Qtotal = zeros(1,600); Tc = zeros(1,600); delta_T = zeros(1,600);Qc = zeros
        (1,600);
343 delta_sag = zeros(1,600); sag_f = zeros(1,600);sag_i = zeros(1,600);
344 CondLength_i = zeros(1,600);CondLength_f = zeros(1,600);alpha_As=zeros
        (1,600);
345 expansion=zeros(1,600);
346
347 for b = 1:3
348 ClosestSegNum(b) = Ind{closestTL(b)};
349 ind = closestTL(b);
```

```
350 [Qj(b,:),Qs(b,:),Qr(b,:),Qc(b,:), Qtotal(b,:),delta_T(b,:),Tc(b,:),sag_f(b
        ,:),delta_sag(b,:), expansion(b,:)] = heatTransferStep(latitude(b),
        buses.lines(ind).azimuth, buses.lines(ind).current, ClosestSpan(b), VF(
        b,:), fArea(1,:));
351 end
352
353 % take out zeros
354 Qj(Qj==0)=nan; Qs(Qs==0)=nan; Qr(Qr==0)=nan; Qc(Qc==0)=nan; Qtotal(Qtotal
        ==0)=nan; expansion(expansion==0)=nan;
355 Tc(Tc==0)=nan; delta_T(delta_T==0)=nan; delta_sag(delta_sag==0)=nan; sag_f(
        sag_f==0)=nan;
```

```
1  function setGlobal
2  global simTime earthRadiusInMeters OD condRadius Towerheight Ta fSpeed N Ns
       F...
3  V_w phi fTemp TcThreshold cs ca ma ms mc emissivity stefan_boltz
      absorptivity...
4  k_sk alpha Rdc He
5
6  simTime = 600;
7  earthRadiusInMeters = 6371000;
8  Ta = randi([20 37],1,1); % ambient temp
9
10 % conductor parameters
11 OD = 21.221/1000;%
12 condRadius = OD/2;
13 cs = 481; % specific heat of steel (J/kg*K)
14 ca = 897; % specific heat of aluminum
15 ms = 0.5119; % mass per unit length for steel (kg/m)
16 ma = 1.116; % mass per unit length for aluminum
17 mc = cs*ms + ca*ma;
18 absorptivity = 0.8; % absorption coefficent of the line; bt 0.2 and 0.9
19
20 % radiative heating parameters
21 emissivity = 0.8;
22 stefan_boltz = 5.6697*10^(-8); % Stefan-Boltzman's constant
23 Towerheight = 32.004;
24 TcThreshold = 660.32; % at 660.32 deg C, it melts AL with steel
25
26 % solar heating parameters
```

```
27 F = 0.1; % ground albedo; 0.1 for forest
28 N = randi([1 365],1,1); % day of the year (1 to 365) julian calendar
29 Ns = 0.1 + (1.2-0.1).*rand(1,1); % clearness ratio; 0 ~ 1.2;
30
31 % joule heating parameters
32 alpha = 0.00403; % resistance temp coefficient (1/deg C)
33 k_sk = 1.01;% skin effect and iron loss factor; less than 1.02 for normal
       OD (<45mm)
34 Rdc = 4.4291*10^(-5); %
35
36 % forced convection parameters
37 V_w = 1; %wind speed in m/s
38 phi = 90; % assumes only perpendicular wind to the conductor
39 He = 100; % elevation of conductor above sea level; assume 100m ground/line
        elevation
40
41 % fire parameters
42 fTemp = 1073.15; % typical fire temp in deg C
43 fSpeed = 0.36; % m/s
44 end
```

```
1  %% heat transfer model without fire
2  function [delta_T,Tc,sag_f,delta_sag] = heatTransferNormal(latitude,
       azimuth_con, Iac, span)
3  global Ta Ns N mc F simTime
4
5  alpha_As = 18.9*10^(-6); % coeff of thermal expansion
6  % preallocation
7  Qj = zeros(1,600); Qs = zeros(1,600); Qr = zeros(1,600); Qc = zeros(1,600);
8  Qtotal = zeros(1,600); Tc = zeros(1,600); delta_T = zeros(1,600);
9  delta_sag = zeros(1,600); sag_f = zeros(1,600);%sag_i = zeros(1,600);
10 CondLength_i = zeros(1,600);CondLength_f = zeros(1,600);expansion=zeros
       (1,600);
11
12 time = 32400; Tc(1) = Ta; delta_t = 0;
13
14 for k = 1:simTime - 1
15 delta_t = delta_t + 1;
16 Qj(k) = CurrentRad(Tc(k), Iac);
17 Qs(k) = SolarRad(time, azimuth_con, latitude);
18 Qr(k) = RadCooling(Ta, Tc(k)); % line to air; this would be cooling
19 Qc(k) = Conv(Ta,Tc(k));
20 Qtotal(k) = Qs(k) + Qj(k) - Qr(k) - Qc(k);
21 delta_T(k) = delta_t*(Qtotal(k)/(mc));
22 Tc(k+1) = Tc(k) + delta_T(k);
23 [expansion(k), sag_f(k), delta_sag(k), CondLength_i, CondLength_f(k)] =
       Sagcalculator(alpha_As, delta_T(k), span);
24
25 if Tc(k) > Ta && Tc(k) <= 250
```

```
26  alpha_As = 2*10^(-9)*Tc(k) + 18.9*10^(-6);
27  else
28  alpha_As = 2*10^(-12)*Tc(k) + alpha_As;
29  end
30  time = time + 1;
31  end
32  end
```

```
1  % heat transfer model without the simulation of the normal heat transfer
2  % model
3  function [Qj,Qs,Qr,Qc,Qtotal,delta_T,Tc,sag_f,delta_sag,expansion] =
       heatTransferStep(latitude, azimuth_con, Iac, span, VF, fArea, dist,
       fRadius)
4  global simTime fTemp TcThreshold mc Ta
5
6  alpha_As = 18.9*10^(-6);
7
8  % preallocation
9  Qj = zeros(1,600); Qs = zeros(1,600); Qr = zeros(1,600); Qc = zeros(1,600);
       Qcf = zeros(1,600);
10 Qtotal = zeros(1,600); Tc = zeros(1,600); delta_T = zeros(1,600);
11 delta_sag = zeros(1,600); sag_f = zeros(1,600);
12 CondLength_i = zeros(1,600);CondLength_f = zeros(1,600);expansion=zeros
       (1,600);
13
14 delta_t = 0; time = 32400; Tc(1) = Ta;
15 for k = 1:simTime - 1 %
16 delta_t = delta_t + 1;
17 Qj(k) = CurrentRad(Tc(k), Iac);
18 Qs(k) = SolarRad(time, azimuth_con, latitude);
19 Qr(k) = RadHeating(Tc(k),fTemp, VF(k), fArea(k)); % fire to line
20 Qc(k) = Conv(Ta,Tc(k));
21 Qcf(k) = Conv(Tc(k),fTemp);
22
23 if fRadius > dist
24 Qtotal(k) = Qr(k)+ Qs(k) + Qj(k) - Qc(k) + Qcf(k);
```

```
25 else
26 Qtotal(k) = Qr(k)+ Qs(k) + Qj(k) - Qc(k);
27 end
28
29 delta_T(k) = delta_t*(Qtotal(k)/(mc));
30 Tc(k+1) = Tc(k) + delta_T(k);
31
32 if Tc(k) >= TcThreshold
33 break
34 end
35
36 if Tc(k) >= 20 && Tc(k) < 100
37 m = (23.6*10^(-6) - 18.9*10^(-6))/(100-20);
38 alpha_As(k) = m*(Tc(k)-20) + 18.9*10^(-6);
39 k1 = k;
40 elseif Tc(k) >= 100 && Tc(k) < 250
41 m = (25.2*10^(-6) - 23.6*10^(-6))/(250-100);
42 alpha_As(k) = m*(Tc(k)-100) + alpha_As(k1);
43 k2 = k;
44 else
45 m = (26.1*10^(-6) - 25.2*10^(-6))/(660-250);
46 alpha_As(k) = m*(Tc(k)-250) + alpha_As(k2);
47 end
48
49 [expansion(k), sag_f(k), delta_sag(k)] = SagcalcFire(alpha_As(k), delta_T(k
      ), span,Tc(k));
50
51 time = time + 1;
```

```
52  end
53
54  end
```

```
1  function [expansion, sag_f, delta_sag] = SagcalcFire(alpha_As, delta_T,
       span, T)
2
3  w = 15.97; % conductor unit weight, N/m; Drake
4  % H_i = 28000; %; %initial horizontal tension, N at 15 deg C ;
5  H_i = -128*T.^2+41.7*T+19.2; % derived equation of the 3-point parabola to
       get conductor tension from temp
6  Area = 468.5*10^(-6); % cond area, m^2
7  E = 73.98*10^9; % Pa
8  epi = 0; % permanent/plastic elongation
9
10 k1 = (1 + (w*span).^2/(24*H_i.^2)) * (1 + (delta_T)*alpha_As)/(Area*E);
11 k2 = (1 + (w*span).^2/(24*H_i.^2)) * (1 + (delta_T)*alpha_As)*(1 - H_i/(
       Area*E) + epi) - 1;
12 k4 = (w*span).^2/24;
13 H = real(roots([k1 k2 0 -k4]));
14 if H(1)>0
15 H_f = H(1);
16 elseif H(2)>0
17 H_f = H(2);
18 else
19 H_f = H(3);
20 end
21
22 CondLength_i = (H_i/w)*sinh(w*span/H_i);
23 expansion = alpha_As*CondLength_i*(delta_T);
24 sag_i = (H_i/w)*(cosh(span*w/(2*H_i))-1);
25 sag_f = (H_f/w)*(cosh(span*w/(2*H_f))-1);
```

```
26  delta_sag = (sag_f - sag_i); % m
27
28  if delta_T <= 0
29  delta_sag = 0;
30  end
31  if sag_f >= 0.05*span
32  sag_f = sag_f + sag_f.^2*w/(6*H_f);
33  end
34  end
```

```
1  %% convective cooling
2  function Qc = Conv(Ti, Tf)
3  global OD V_w phi He
4  Tfilm = 0.5*(Ti+Tf);
5  mu_f = (1.458*10^(-6)*((Tfilm+273).^1.5))/(Tfilm+383.4); % wiscosity of air
6  rho_f = (1.293-1.525*10^(-4)*He+6.379*10^(-9)*He.^2)/(1+0.00367*Tfilm);
7  N_RE = (OD*1000) * rho_f * V_w/mu_f; % Reynolds number;
8  Kangle = 1.194 - cosd(phi) + 0.194*cosd(2*phi) + 0.368*sind(2*phi); % wind
       direction factor
9  k_f = 2.424*10^(-2) + 7.477*10^(-5)*Tfilm - 4.407*10^(-9)*Tfilm.^2;
10 Qc1 = (1.01+0.0372*N_RE.^0.52)*k_f*Kangle*(Tf-Ti);
11 Qc2 = (0.0119*N_RE.^0.6)*k_f*Kangle*(Tf-Ti);
12 if Qc1 >= Qc2
13 Qc = Qc1;
14 else
15 Qc = Qc2;
16 end
17 end
```

```
1  %% radiative cooling from line to sky
2  function Qrc = RadCooling(Tinitial, Tfinal)
3  global stefan_boltz OD
4  emissivity = 0.5; % emissivity
5  Qrc = pi*OD*emissivity*stefan_boltz*((Tfinal + 273.15).^4 - (Tinitial +
       273.15).^4);
6  if Tinitial >= Tfinal
7  Qrc = 0;
8  end
9  end
```

```
1 %% radiative heating between fire and line
2 function Qr = RadHeating(Tinitial, Tfinal, ViewFactor, fArea)
3 global stefan_boltz emissivity
4 Qr = fArea*ViewFactor*emissivity*stefan_boltz*((Tfinal + 273.15).^4 - (
      Tinitial + 273.15).^4); % here fArea dominates
5 end
```

```
1 %initialize the fire as a circle and gets the coordinates for view factor
2 function [fArea, fCoords] = FireCalc(fRadius)
3 fArea = pi*(fRadius.^2);
4 M = 120; % number of sides of polygon
5 [X,Y,Z] = cylinder(fRadius,M); % fire coordinates
6 Z = Z+1.8; %fire height of 1.8 m;
7 fCoords = [X(1,1:M-1)',Y(1,1:M-1)',Z(1,1:M-1)']; % Coords of the vertices
8 end
```

```
1  %% solar radiation
2  function Qs = SolarRad(time, azimuth_con, latitude)
3  global OD absorptivity F N Ns
4
5  second_angle = 0.00416*(43200-time); % second angle of the sun;
6  declination = 23.3*sind(2*pi*(284+N)/365); % declination (deg)
7  altitude = asind(sind(latitude)*sind(declination) + cosd(latitude)*cosd(
       declination)*cosd(second_angle)); % solar altitude
8  if altitude < 0
9  altitude = 0;
10 end
11
12 Ib = Ns*1280*sind(altitude)/(sind(altitude)+0.314); % direct solar
       radiation at sea level
13 Id = (430.5-0.3288*Ib)*sind(altitude); % diffuse solar radiation intensity
       (W/m^2)
14 azimuth_sun = asind(cosd(declination)*sind(second_angle)/cosd(altitude)); %
        azimuth of the sun in deg
15 eta = acosd(cosd(altitude)*cosd(azimuth_sun-azimuth_con)); % angle of solar
        beam wrt axis of conductor(deg)
16 It = Ib*(sind(eta)+pi*F*sind(altitude)/2) + Id*(1+pi*F/2); % global
       radiation intensity
17 Qs = absorptivity*It*OD;
18 end
```

```
1 %% current/Joule heating for steel cored conductors
2 function Qj = CurrentRad(Tc, Iac)
3 global k_sk Ta alpha Rdc
4 Qj = (Iac.^2)*k_sk*Rdc*(1+alpha*(Tc-Ta));
5 end
```

```
1 %% calculates midpoint between two points
2 function m = midPoint(p1,p2)
3 m = [((p1(1)+p2(1))/2), ((p1(2)+p2(2))/2)];
4 end
```

Appendix B

LOAD FLOW SINGLE LINE ON ETAP

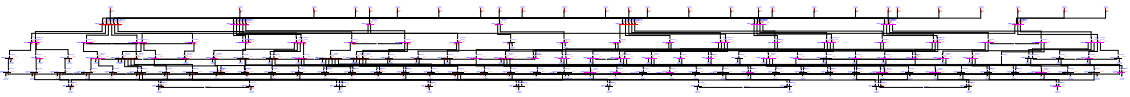

Appendix C

BLOCK DIAGRAMS OF A LINE SAG SENSOR

Figure C.1: Level 0 Block Diagram of a Line Sag Sensor.

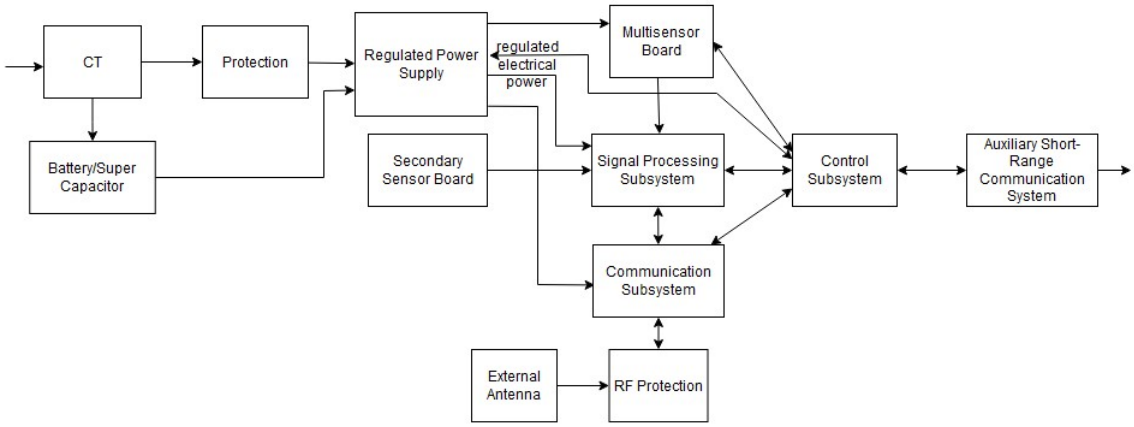

Figure C.2: Level 1 Block Diagram of a Line Sag Sensor.

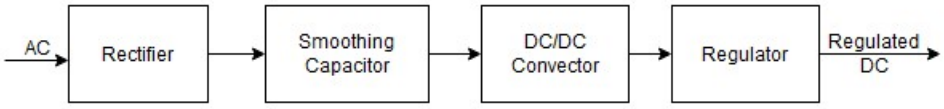

Figure C.3: Level 2 Block Diagram of the Regulated Power Supply in the Sensor.

Appendix D

BEHAVEPLUS SETTINGS

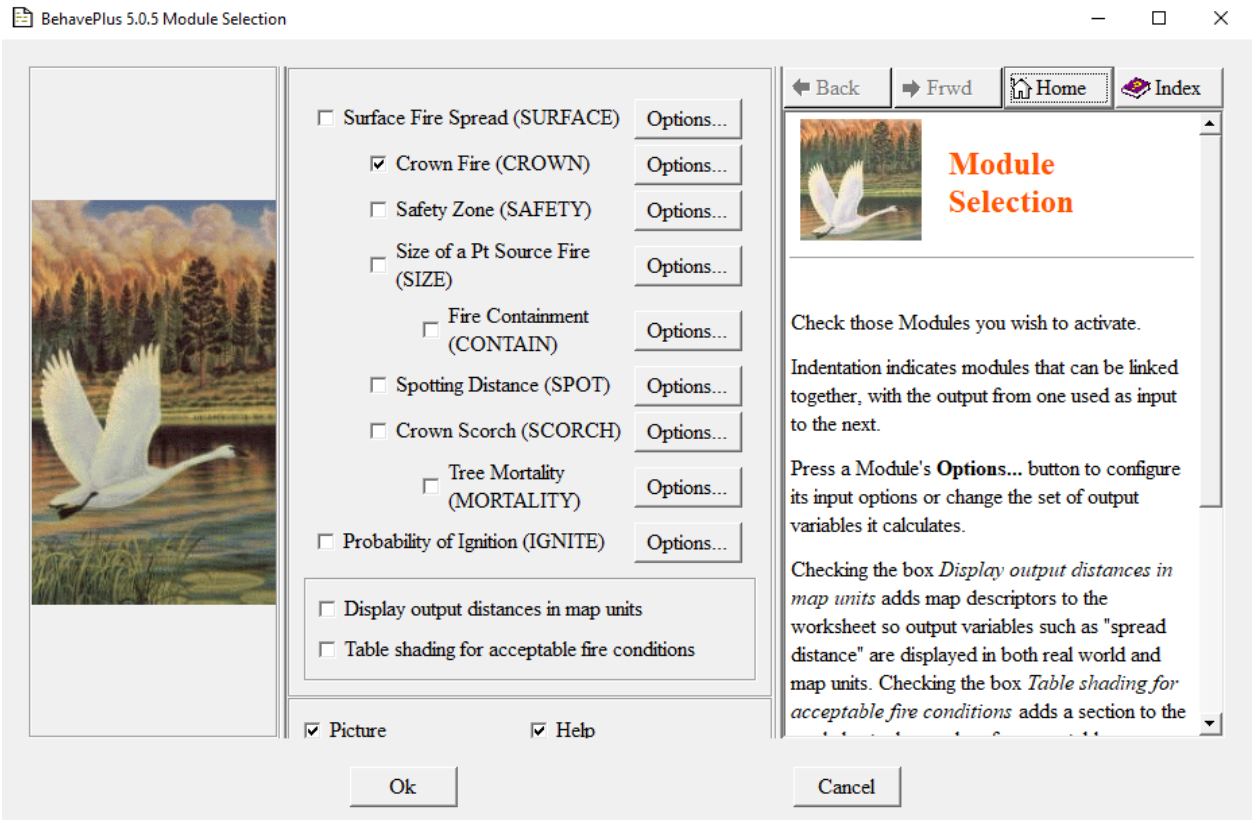
BehavePlus 5.0.5 Module Selection
Surface Fire Spread (SURFACE)
Options...
Crown Fire (CROWN)
Options...
Safety Zone (SAFETY)
Options...
Size of a Pt Source Fire (SIZE)
Options...
Fire Containment (CONTAIN)
Options...
Spotting Distance (SPOT)
Options...
Crown Scorch (SCORCH)
Options...
Tree Mortality (MORTALITY)
Options...
Probability of Ignition (IGNITE)
Options...
Display output distances in map units
Table shading for acceptable fire conditions
Picture
Help
Ok
Cancel
Back
Frwd
Home
Index
Module Selection
Check those Modules you wish to activate.
Indentation indicates modules that can be linked together, with the output from one used as input to the next.
Press a Module's Options... button to configure its input options or change the set of output variables it calculates.
Checking the box Display output distances in map units adds map descriptors to the worksheet so output variables such as "spread distance" are displayed in both real world and map units. Checking the box Table shading for acceptable fire conditions adds a section to the

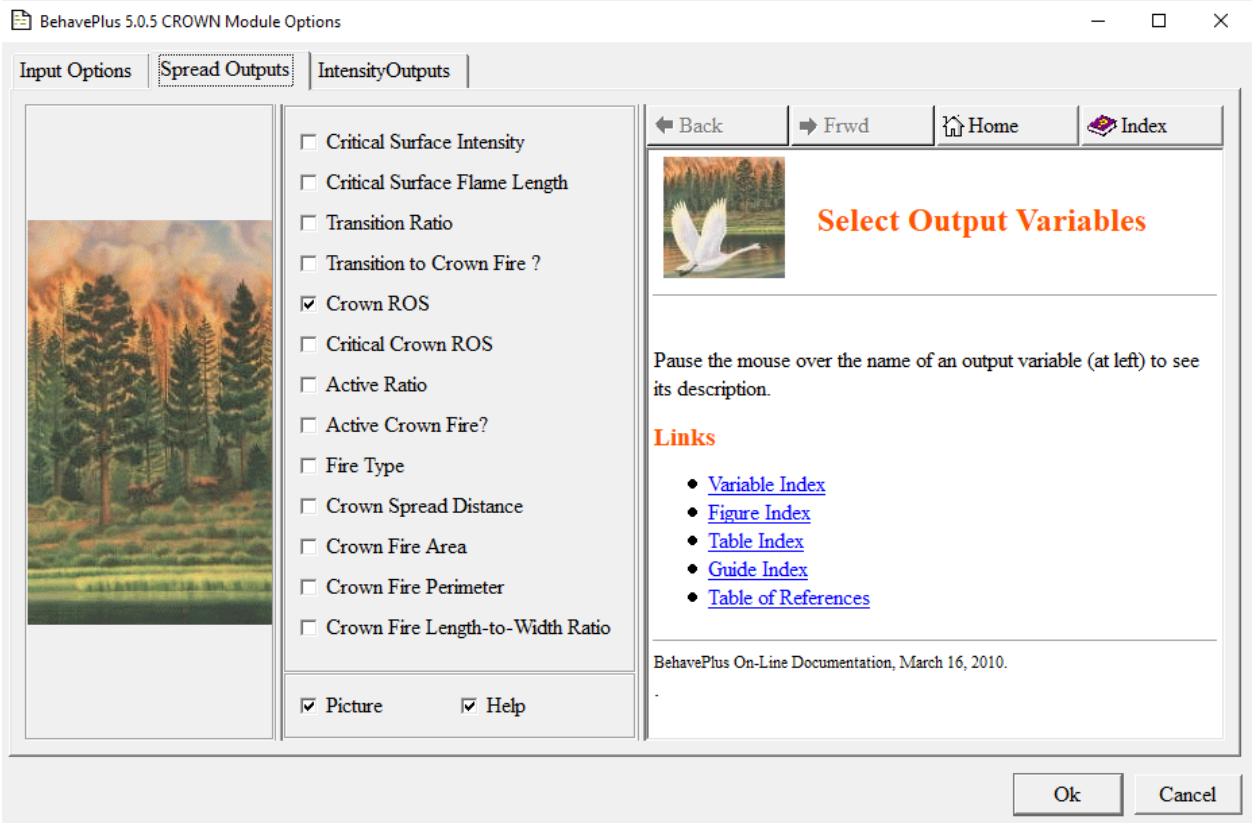
BehavePlus 5.0.5 CROWN Module Options
Input Options
Spread Outputs
IntensityOutputs
Critical Surface Intensity
Critical Surface Flame Length
Transition Ratio
Transition to Crown Fire ?
Crown ROS
Critical Crown ROS
Active Ratio
Active Crown Fire?
Fire Type
Crown Spread Distance
Crown Fire Area
Crown Fire Perimeter
Crown Fire Length-to-Width Ratio
Picture
Help
Ok
Cancel
Back
Frwd
Home
Index
Select Output Variables
Pause the mouse over the name of an output variable (at left) to see its description.
Links
Variable Index
Figure Index
Table Index
Guide Index
Table of References
BehavePlus On-Line Documentation, March 16, 2010.

Inputs: CROWN

Description		Crown Fire Rate of Spread

Fuel Moisture

1-h Moisture	%	4
10-h Moisture	%	5
100-h Moisture	%	6
Live Woody Moisture	%	40, 60, 80, 100

Weather

20-ft Wind Speed (upslope)	km/h	0, 5, 10, 15, 20

Run Option Notes

None

Output Variables

Crown ROS (m/min) [CROWN]

Notes

BehavePlus 5.0.5 Calculate Results

☑ Display table results

Select the Table Row Variable

○ Live Woody Moisture

◉ 20-ft Wind Speed (upslope)

☑ Display graph results

Select the X-Axis Variable

○ Live Woody Moisture

◉ 20-ft Wind Speed (upslope)

☐ Specify graph Y axis limits

☑ Picture

Tables

Two input variables have multiple values:

- Live Woody Moisture
- 20-ft Wind Speed (upslope)

Select one of them to be the table's *row* variable.

The unselected one will be the table's *column* variable.

A separate table will be produced for each output variable.

Graphs

Ok

Cancel